





# Circadian time- and sleep-dependent modulation of cortical parvalbumin-positive inhibitory neurons

Fang-Jiao Zong<sup>1,2,†</sup> , Xia Min<sup>1,2</sup>, Yan Zhang<sup>3</sup> , Yu-Ke Li<sup>1,2</sup>, Xue-Ting Zhang<sup>1,2</sup>, Yang Liu<sup>1,2</sup>  & Kai-Wen He<sup>1,2,\*</sup> 

## Abstract

Parvalbumin-positive neurons (PVs) are the main class of inhibitory neurons in the mammalian central nervous system. By examining diurnal changes in synaptic and neuronal activity of PVs in the supragranular layer of the mouse primary visual cortex (V1), we found that both PV input and output are modulated in a time- and sleep-dependent manner throughout the 24-h day. We first show that PV-evoked inhibition is stronger by the end of the light cycle (ZT12) relative to the end of the dark cycle (ZT0), which is in line with the lower inhibitory input of PV neurons at ZT12 than at ZT0. Interestingly, PV inhibitory and excitatory synaptic transmission slowly oscillate in opposite directions during the light/dark cycle. Although excitatory synapses are predominantly regulated by experience, inhibitory synapses are regulated by sleep, via acetylcholine activating M1 receptors. Consistent with synaptic regulation of PVs, we further show *in vivo* that spontaneous PV activity displays daily rhythm mainly determined by visual experience, which negatively correlates with the activity cycle of surrounding pyramidal neurons and the dorsal lateral geniculate nucleus-evoked responses in V1. These findings underscore the physiological significance of PV's daily modulation.

**Keywords** daily rhythm; neural activity; parvalbumin; sleep; synaptic transmission

**Subject Categories** Neuroscience; Signal Transduction

**DOI** 10.15252/embj.2022111304 | Received 30 March 2022 | Revised 13 October 2022 | Accepted 4 November 2022 | Published online 7 December 2022

**The EMBO Journal (2023) 42: e111304**

## Introduction

Parvalbumin (PV)-expressing GABA ( $\gamma$ -aminobutyric acid)-ergic neurons are the most abundant class of inhibitory neurons in the neocortex (Rudy *et al*, 2011). By forming dense inhibitory connections around soma or the axon initial segment of their neighboring neurons, mainly glutamatergic principal neurons, these fast-spiking inhibitory neurons gate the excitability of their targets and play

critical roles in maintaining the stability as well as enhancing the computational power and precision of the neural network (Hu *et al*, 2014; Ferguson & Cardin, 2020; Sadeh & Clopath, 2021). For example, in the primary visual cortex (V1), PV neurons are known to control cortical plasticity (Sur *et al*, 2013; van Versendaal & Levelt, 2016) and visual response properties such as response gain (Atallah Bassam *et al*, 2012; Wilson *et al*, 2012; Zhu *et al*, 2015). Furthermore, dysregulation of PV neurons is tightly associated with a variety of brain disorders, such as epilepsy (Wang *et al*, 2017), autism (Vogt *et al*, 2018), schizophrenia (Steullet *et al*, 2017), and Alzheimer's disease (AD; Hijazi *et al*, 2019). Thus, defining the functional regulation of PV neurons will provide important insight into their roles in normal and diseased brains.

Despite their functional importance, how PV neurons are modulated remains poorly understood. Most studies have focused on the impacts of disease-associated genetic mutations on early development of PV neurons (Marin, 2012; Hu *et al*, 2017), which provides insight into the cause of defects in these diseases. But for other psychiatric and neurodegenerative disorders, very little is known about how dysregulation of PV neurons might occur. Recent studies showed that early-life sleep may regulate the neurodevelopment of cortical PV neurons (Jones *et al*, 2019). In mature brain, different sleep/wake stages and sleep history are reported to acutely affect the spontaneous firing of both excitatory and inhibitory neurons (Vyazovskiy *et al*, 2009; Miyawaki & Diba, 2016) including PV neurons (Niethard *et al*, 2016), although contradictory results exist (Hengen *et al*, 2013, 2016). These findings suggest sleep may be crucial for PV neurons' regulation. We previously reported that the excitation/inhibition (E/I) ratio of cortical pyramidal neurons naturally changes during the 24-h day, of which the synaptic inhibition oscillates dramatically and is influenced by sleep (Bridi *et al*, 2020). Taken together, we hypothesized that cortical PV neurons might be dynamically modulated daily. Whether and how this happens and what physiological effects it may have are questions of importance that might shed light on the functional regulation of PV neurons.

We studied the above questions in V1 by combining *ex vivo* and *in vivo* assessments. We first observed that the inhibitory output from PV neurons indeed dramatically differs between the light and dark cycle. Consistently, we found that PV's excitatory and

<sup>1</sup> Interdisciplinary Research Center on Biology and Chemistry, Shanghai Institute of Organic Chemistry, Chinese Academy of Sciences, Shanghai, China

<sup>2</sup> University of Chinese Academy of Sciences, Beijing, China

<sup>3</sup> Shanghai Open University, Shanghai, China

\*Corresponding author. Tel: +86 021 68582320; E-mail: kwhe@sioc.ac.cn

<sup>†</sup>Present address: Qingdao University School of Pharmacy, Qingdao, China

inhibitory synaptic transmission slowly oscillates in the opposite direction during the 24-h day. In addition to the time dependency, we found that experience dominates the regulation of PV's synaptic excitation while sleep plays an essential role in regulating PV's synaptic inhibition. We further identified acetylcholine (ACh) via targeting presynaptic M1R is required for the daily regulation of PV's synaptic inhibition. In line with all the *ex vivo* changes, we observed a daily oscillation in PV's spontaneous activity *in vivo* strongly dependent on visual experience. At last, we found that the activity of putative pyramidal neurons in V1 oscillates in the opposite direction as PV neurons. Furthermore, we demonstrated that direct dorsal lateral geniculate nucleus (dLGN) stimulation evoked neuronal activities in V1, which mimics vision-evoked responses, are stronger at ZT0 compared to ZT12. This pattern is consistent with PV's role in gain control, further strengthening the physiological importance of this novel mode of daily modulation of PV neurons.

## Results

### Altered PV-evoked inhibition onto pyramidal neurons between the light and dark cycle

We previously found that the inhibitory synaptic transmission of V1 L2/3 pyramidal neurons slowly increases and remains high during the light cycle and gradually reduces and remains low during the dark cycle (Bridi *et al.*, 2020). Therefore, we hypothesized that altered inhibitory output from PV neurons contribute to this phenomenon. Using PV:Ai32 transgenic mice expressing channelrhodopsin-2 (ChR2) specifically in PV neurons, we directly recorded light-evoked inhibitory postsynaptic currents ( $_{LE}$ IPSCs) in V1 L2/3 pyramidal neurons at the end of the light cycle (Zeitgeber time 12, ZT12) and the end of dark cycle (ZT0; Fig 1A and Appendix Fig S1A, see [Materials and Methods](#)). In V1-containing acute brain slices, we sub-divided a cubic area of 0.45 mm<sup>2</sup> covering L1 to L5 of V1 into 15 by 15 grids (Fig 1A<sub>3</sub>). The soma position of the recorded pyramidal neurons was relatively fixed. Each grid was sequentially stimulated with brief blue light pulse in a pseudorandom order and pharmacologically isolated, light-evoked inhibitory postsynaptic currents ( $_{LE}$ IPSCs) were recorded from L2/3 pyramidal neurons by voltage clamped at -50 mV. We only analyzed  $_{LE}$ IPSCs with short latency, high fidelity and maximal amplitude larger than 60 pA (see [Materials and Methods](#)). We used the maximal amplitude of the  $_{LE}$ IPSCs as pixel value for corresponding grid and plotted a two-dimensional map for each pyramidal neuron (Fig 1A<sub>5</sub>, see [Materials and Methods](#)). We first compared the IPSC strength by aligning all maps from each group according to the soma position of the recorded neuron. The averaged soma-aligned map of ZT12 shows higher signal intensity than ZT0 (Fig 1B).  $_{LE}$ IPSCs at ZT12 were significantly larger (both max amplitude and summation of all currents) compared to those at ZT0 (Fig 1C and D). The difference between ZT0 and ZT12 was unlikely caused by variant levels of ChR2 since we randomly recorded PV: Ai32 mice from the same litter at ZT0 or ZT12, and the differences were highly conserved among all litters (Appendix Fig S1B). These results support our hypothesis that the functional output from cortical PV neurons varies at different times of the day—high at ZT12 while low at ZT0.

To further investigate whether the spatial distribution of PV-evoked inhibition was also altered between ZT0 and ZT12, we projected each map onto the reference map (Fig 1A<sub>3</sub>) after pia alignment (pia-align, see [Materials and Methods](#)). The averaged pia-aligned maps of both groups show that the  $_{LE}$ IPSCs were mainly evoked within L2/3 with similar lateral distribution between groups (Fig 1E). In the vertical direction, a significant proportion of IPSCs was also evoked from L4, but relatively weak from L5, and the distribution seems to be flattened at ZT12 (Fig 1E). While pyramidal neurons recorded in both groups had similar spatial distribution (Appendix Fig S1C and D), their input size was significantly larger at ZT12 than at ZT0 (Fig 1F), suggesting PV neurons from broader area might be recruited at ZT12. Thus, these results in combine suggest that PV's output indeed alters markedly at different times of the day.

### Opposite oscillation of excitatory and inhibitory synaptic transmission of PV neurons during the light/dark cycle

Changes in PV and pyramidal neuron's intrinsic excitability or presynaptic properties unlikely contribute to the altered PV-evoked output since both of them are found to be unchanged between the light and dark cycle (Bridi *et al.*, 2020). Inhibition is known to gate neuronal output (Gidon & Segev, 2012; Jelitai *et al.*, 2016), we therefore examined whether PV neurons received different inhibition between ZT0 and ZT12. We recorded miniature inhibitory postsynaptic currents (mIPSCs) of V1 L2/3 PV neurons from acute brain slices harvested at either ZT0 or ZT12. Indeed, mIPSC frequency was significantly reduced at ZT12 compared to ZT0 (Fig 2B) with unaltered amplitude (Fig 2D). These results indicate that PV neurons are less suppressed at ZT12, which might underlie the greater PV-evoked inhibitory output. We previously found that the synaptic excitation and inhibition of cortical pyramidal neurons are modulated daily (Bridi *et al.*, 2020). We therefore wondered whether the excitation of PV neurons is also modulated during the light/dark cycle. Interestingly, mEPSC frequency but not amplitude was higher at ZT12 than at ZT0 (Fig 2A and C), suggesting that PV neurons receive more excitatory inputs by the end of the light cycle.

To further evaluate the temporal profile of PV's synaptic transmission, we recorded PV's spontaneous EPSCs and IPSCs that are more physiologically relevant (Jurgensen & Castillo, 2015) at multiple time points during the light/dark cycle (Fig 3A). Similar to miniature currents, both sEPSCs and sIPSCs changed but in the opposite direction. Specifically, sEPSCs and sIPSCs were increased and decreased respectively 4 h after entering the light cycle, then they were maintained relatively stable between ZT4 and ZT12. Similar changes but in the opposite direction occurred after switching into the dark cycle, resulting in clear rhythmic oscillations during the 24-h day (Fig 3B and C). Thus, PV's synaptic excitation and inhibition are modulated in a time-dependent manner during the light/dark cycle.

### Experience- and sleep-dependent regulation of synaptic transmission of PV neurons

We next sought to understand what may drive the opposite changes in PV's excitation and inhibition. Neurons including GABAergic inhibitory neurons in V1 L2/3 are strongly recruited

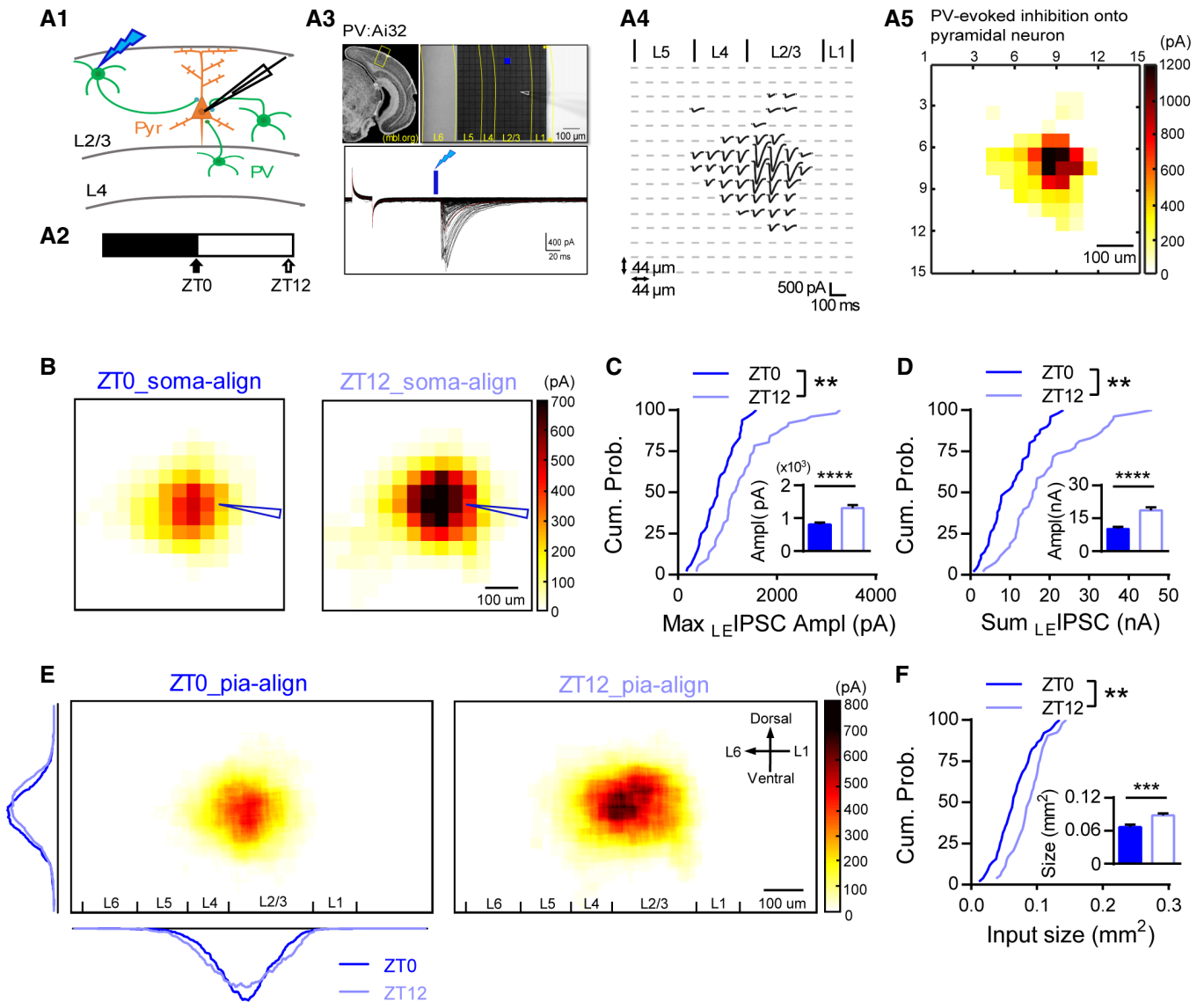


**Figure 1. Distinct inhibitory output from PV neurons between the light and dark cycle.**

- A Experimental demonstration. A<sub>1</sub>. Illustration of the mapping principle between ChR2-expressed PV neurons (green) and regular pyramidal neuron (Pyr, orange). A<sub>2</sub>. Acute slices were obtained and recorded at ZT0 or ZT12. A<sub>3</sub>. Coronal brain atlas showing the primary visual cortex (Top left panel, modified from MBL mouse brain atlas). Yellow box highlights the region of experiment. Top right panel, the reference image taken with a 10× objective from a slice prepared from a PV: Ai32 mouse. The 0.45 mm<sup>2</sup> shaded cubic area was divided into 15 × 15 grids for independent light stimulation. The white arrowhead indicates the position of the recording electrode. Bottom panel, representative raw traces of light-evoked IPSCs (LEIPSCs) recorded from one pyramidal neuron. A<sub>4</sub>. The spatial distribution of the LEIPSCs from the example in (A<sub>3</sub>). A<sub>5</sub>. The heatmap of the LEIPSCs in (A<sub>4</sub>).
- B The average heatmaps at ZT0 and ZT12 after soma alignment. Soma position was indicated by the blue arrow head.
- C Comparison of the cumulative distribution (Kolmogorov–Smirnov test [K-S test];  $P = 0.002$ ) and the mean (Inset: ZT0: 813.3 ± 53.13 pA; ZT12: 1306 ± 93.73 pA;  $P < 0.0001$ ; Mann–Whitney  $U$  test) of the max LEIPSC amplitude between ZT0 and ZT12.
- D Comparison of the cumulative distribution (K-S test,  $P = 0.0016$ ) and the mean (Inset: ZT0: 10.44 ± 1.44 nA; ZT12: 18.87 ± 1.44 nA;  $P < 0.0001$ ; Mann–Whitney  $U$  test) of the sum LEIPSC amplitude between ZT0 and ZT12.
- E The average heatmaps of LEIPSCs after pia alignment to the reference image in (A<sub>3</sub>). Dark and light blue overlay traces on the side of the map depicted the marginal distribution of the sum LEIPSCs for ZT0 (Dark blue) and ZT12 (Light blue).
- F Comparison of the cumulative distribution (K-S test,  $P = 0.0021$ ) and the mean (Inset: ZT0: 0.067 ± 0.004 mm<sup>2</sup>; ZT12: 0.089 ± 0.0036 mm<sup>2</sup>;  $P = 0.0003$ ; Mann–Whitney  $U$  test) inhibitory input size between ZT0 and ZT12.

Data information: Sample sizes used in this figure: ZT0: 48 cells from nine mice; ZT12: 51 cells from nine mice. Error bars in all figures indicate standard error of mean (s.e.m). The level of significance was set at  $P < 0.05$ . \* $P < 0.05$ ; \*\* $P < 0.01$ ; \*\*\* $P < 0.001$ ; \*\*\*\* $P < 0.0001$ .

Source data are available online for this figure.

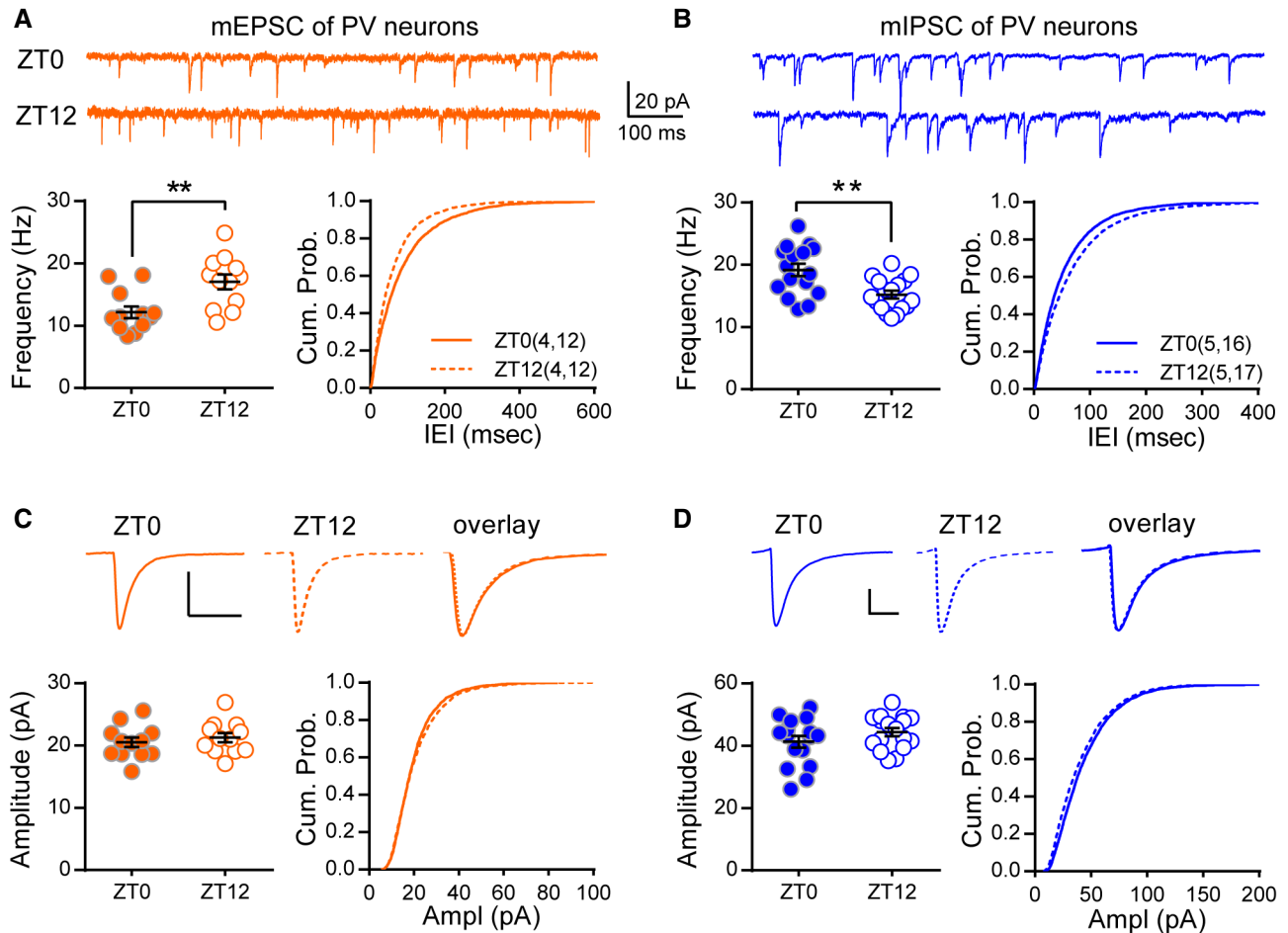


**Figure 2. Opposite modulation of the excitatory and inhibitory synapses onto PV neurons during the light/dark cycle.**

**A** mEPSC frequency was higher at ZT12 than ZT0. Top: example traces of mEPSC recordings. Bottom left: mEPSC frequency (ZT0:  $12.17 \pm 0.94$  Hz; ZT12:  $17.03 \pm 1.20$  Hz;  $P = 0.0036$ ; Mann–Whitney  $U$  test). Bottom right: cumulative probability histogram of the inter-event intervals ( $K$ -S test,  $P < 0.0001$ ).

**B** mIPSC frequency was lower at ZT12 than ZT0. Top: example traces. Bottom left: mIPSC frequency (ZT0:  $19.15 \pm 0.99$  Hz; ZT12:  $15.19 \pm 0.63$  Hz;  $P = 0.0042$ ; Mann–Whitney  $U$  test). Bottom right: cumulative probability histogram of the inter-event intervals of mIPSCs ( $K$ -S test,  $P < 0.0001$ ).

**C** mEPSC amplitude and kinetics did not differ between ZT0 and ZT12. Top: average traces of the well-isolated events. Bottom left: mEPSC amplitude (ZT0:  $20.51 \pm 0.78$  pA; ZT12:  $21.26 \pm 0.75$  pA;  $P = 0.34$ ; Mann–Whitney  $U$  test). Bottom right: The distribution of mEPSC amplitude of all events ( $K$ -S test,  $P < 0.01$ ).

**D** mIPSC amplitude and kinetics did not differ between ZT0 and ZT12. Top: average traces of the well-isolated mIPSCs. Bottom left: mIPSC amplitude (ZT0:  $41.31 \pm 1.91$  pA; ZT12:  $44.39 \pm 1.31$  pA;  $P = 0.35$ ; Mann–Whitney  $U$  test). Bottom right: The cumulative distribution of mIPSC amplitudes ( $K$ -S test,  $P < 0.0001$ ).

Data information: Sample size is indicated as (mice, cells). Error bars in all figures indicate standard error of mean (s.e.m). The level of significance was set at  $P < 0.05$ . \* $P < 0.05$ ; \*\* $P < 0.01$ .

Source data are available online for this figure.

and tuned by direct visual experience (Liu *et al.*, 2009; Kerlin *et al.*, 2010). Therefore, visual experience during the light cycle might be involved. To directly test the role of experience, we visually deprived a group of PV: Ai9 mice by dark exposure during the last light cycle prior to experimentation (Dark-ZT12, Fig 3D). Such brief dark exposure barely affects the activity pattern of mice (Faradji-Prevautelet *et al.*, 1990) but completely abolished the upregulation of sEPSCs (Fig 3E), suggesting that experience plays an important role in regulating the excitatory input onto PV neurons. This sort of regulation was not limited to the primary visual cortex. In primary motor cortex (M1), PV neurons showed higher excitatory synaptic transmission by the end of the dark cycle

(Appendix Fig S2B), during which mice are more active, further supporting the experience dependency. In striking contrast, we found that the downregulation of IPSC during the light cycle was independent of visual input (Fig 3F), indicative of distinct regulatory mechanisms for PV's synaptic excitation and inhibition during the light/dark cycle. Sleep has been shown to regulate both excitation and inhibition of pyramidal neurons (Liu *et al.*, 2010; Bridi *et al.*, 2020). Therefore, we next studied how acute sleep deprivation (SD) at the beginning of the light cycle may affect PV's synaptic transmissions (Fig 3G), during which mice spend around 70% of time sleeping (Appendix Fig S2C). SD was achieved by gentle handling that caused variable but not significant change in plasma

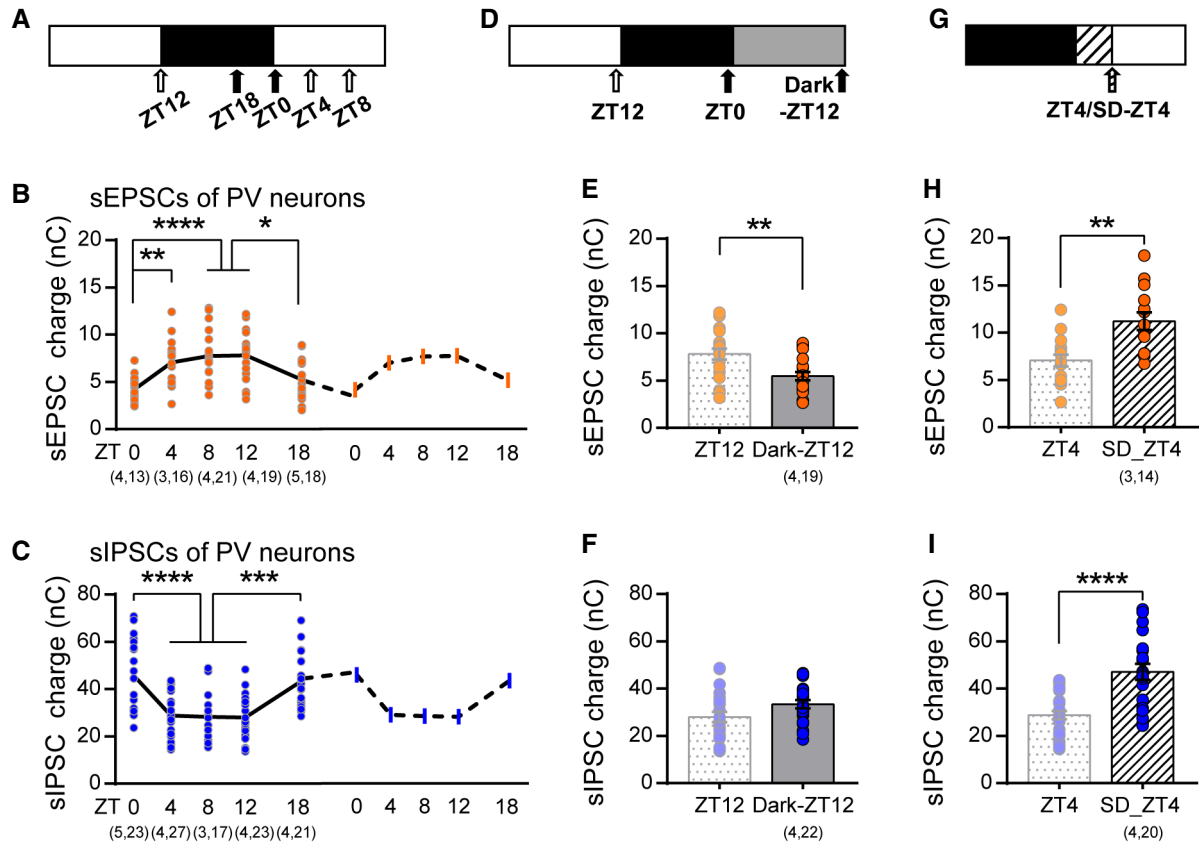


**Figure 3. The excitatory and inhibitory synaptic transmission of PV neurons are modulated by experience and sleep.**

- A Paradigm of experiment. Acute brain slices were obtained at five different times of day (arrowheads).
- B Charges of sEPSCs recorded at light phase were higher compared to those at dark phase (ZT0:  $4.21 \pm 0.28$  nC; ZT4:  $7.05 \pm 0.61$  nC; ZT8:  $7.74 \pm 0.63$  nC; ZT12:  $7.81 \pm 0.59$  nC; ZT18:  $5.25 \pm 0.53$  nC; One-way ANOVA,  $F(4,88) = 8.78$ ,  $P < 0.0001$ , Holm-Sidak post-hoc analysis). A copy of the 24-h sEPSCs was drawn with a dashed line to demonstrate the daily rhythm.
- C Charges of sIPSCs oscillate during the light/dark cycle (ZT0:  $45.73 \pm 2.99$  nC; ZT4:  $28.85 \pm 1.76$  nC; ZT8:  $28.25 \pm 2.77$  nC; ZT12:  $28.04 \pm 2.15$  nC; ZT18:  $43.37 \pm 2.42$  nC; One-way ANOVA,  $F(4,106) = 13.65$ ,  $P < 0.0001$ , Holm-Sidak post-hoc analysis). A copy of the 24-h sEPSCs was drawn with a dashed line to demonstrate the daily rhythm.
- D Paradigm of dark exposure.
- E Dark exposure prevented the increase in sEPSCs that normally occurs at ZT12 (ZT12 as reported in (B); Dark-ZT12:  $5.46 \pm 0.43$  nC;  $P = 0.0082$ ; Mann-Whitney  $U$  test).
- F Dark exposure did not significantly affect the reduction of sIPSCs (ZT12 as reported in (C); Dark-ZT12:  $33.43 \pm 1.74$  nC;  $P = 0.07$ ; Mann-Whitney  $U$  test).
- G Paradigm of acute sleep deprivation (SD).
- H SD further increased sEPSCs compared to *ad lib* sleep mice (ZT4 as reported in (B); SD-ZT4:  $11.22 \pm 0.92$  nC;  $P = 0.0013$ ; Mann-Whitney  $U$  test).
- I SD abolished the reduction of sIPSC (ZT4 as reported in (C); SD-ZT4:  $47.13 \pm 3.39$  nC;  $P < 0.0001$ ; Mann-Whitney  $U$  test).

Data information: Sample size is indicated as (mice, cells). Error bars in all figures indicate standard error of mean (s.e.m). The level of significance was set at  $P < 0.05$ .

\* $P < 0.05$ ; \*\* $P < 0.01$ ; \*\*\* $P < 0.001$ ; \*\*\*\* $P < 0.0001$ .

Source data are available online for this figure.

corticosterone level (Appendix Fig S2F), whose efficacy was confirmed by electroencephalogram (EEG) and electromyogram (EMG) recordings (Appendix Fig S2E). SD abolished the reduction in sIPSCs (Fig 3I), indicating that sleep is required for the down-regulation of synaptic inhibition during the early light cycle. Interestingly, SD failed to prevent the increase, and actually further enhanced sEPSCs (Fig 3H), which is likely due to an additional increase in visual experience indirectly caused by SD. Indeed, this increment was largely abolished by SD in darkness (Appendix Fig S2G), confirming the dominant role of experience in regulating excitatory synapses onto PV neurons. Thus, synaptic

excitation and inhibition of PV neurons are mainly regulated by experience and sleep during the day, respectively.

#### ACh regulates properties of inhibitory synapses onto PV neurons via M1R

Having established that, in contrast to excitation, PV's inhibition is modulated in a time- and sleep-dependent manners, we sought to define the mechanism underlying this process. Changes in mIPSC frequency are usually attributed to either altered presynaptic function or synapse number (Han & Stevens, 2009). By examining



GAD65-positive presynaptic puncta around the soma of PV neurons (Appendix Fig S3A), we found no change in perisomatic inhibitory synaptic density between ZT0 and ZT12 (Appendix Fig S3B<sub>1</sub>), but we did see a decrease in puncta size at ZT12 (Appendix Fig S3B<sub>2</sub>). Positive correlation between presynaptic size and presynaptic function has been reported (Murthy *et al*, 2001). Therefore, our structural results imply that the inhibitory presynaptic function of PV neurons may be rhythmically modulated.

Several neuromodulators including ACh and norepinephrine (NE) have been shown to directly regulate presynaptic properties of different cell types in various brain regions (Kruglikov & Rudy, 2008; Choy *et al*, 2018). Cortical levels of these neuromodulators oscillate during the 24-h day that correlate with the sleep/wake cycle—high during wake cycle and low during sleep cycle (Kametani & Kawamura, 1991; Jiménez-Capdeville & Dykes, 1993), and they are proposed to be the key mediators of circadian rhythm (Frank & Cantera, 2014) and sleep (Tononi & Cirelli, 2014) in regulating synaptic plasticity. To test whether ACh and NE are required for the daily regulation of PV's inhibitory synaptic transmission (Fig 4A), we first tested the effect of cholinergic and noradrenergic agonists on mIPSCs at ZT12, when mIPSC frequency was low (Fig 2B). Whereas treatment with NE was effectless (Appendix Fig S3C), incubation with carbachol (CARB), a non-selective ACh receptor agonist, significantly increased mIPSC frequency (Fig 4B) without changing the amplitude (Fig 4C). This effect was limited to cells recorded at ZT12 but not at ZT0 (Fig 4D and E), indicating that the cholinergic receptors are already activated at ZT0. Interestingly, the effect of ACh seems to be cell type-specific since mIPSCs of pyramidal neurons were insensitive to CARB treatment (Appendix Fig S3H). These results suggest that ACh plays a unique role in the daily regulation of PV's inhibition. To investigate the downstream effector of ACh, we acutely infused brain slices with either muscarinic or nicotinic ACh receptor antagonists after establishing a baseline mIPSC recording at ZT0. Infusion with 50  $\mu$ M non-selective mAChRs antagonist atropine (Atr) but not nAChRs antagonist mecamylamine (MEC; Appendix Fig S3F) was sufficient to reduce mIPSC frequency (Fig 4F), which could be rapidly reversed by washing out the drug (Appendix Fig S3E<sub>1</sub>). Together, these results suggest that the increase in PV's inhibition by the end of the dark cycle requires mAChRs activation. We further defined the subtype of mAChRs by testing antagonists selective for M1R (pirenzepine, Pir) and M3R (1,1-dimethyl-4-diphenylacetoxypiperidinium iodide, 4-DAMP). Pir showed a quick and reversible effect on mIPSC frequency (Fig 4H) similar to Atr but 4-DAMP had no effect (Appendix Fig S3G), suggesting a selective role for M1R. We confirmed these findings by demonstrating that co-incubation with Pir blocked the CARB-induced elevation in mIPSC frequency at ZT12 (Fig 4J). None of these drug treatments affected mIPSC amplitude (Fig 4G, I and K and Appendix Fig S3C<sub>2</sub>–G<sub>2</sub>), further supporting the presynaptic locus for this form of modulation.

How does activation of M1R by ACh alter presynaptic properties? KCNQ potassium channels are downstream targets of M1R activation that influence the membrane potential (Wang & Li, 2016; Appendix Fig S4A) and regulate synaptic release of multiple neurotransmitters including GABA (Martire *et al*, 2004). By testing the effects of KCNQ2/3 channel opener retigabine (PAM; Martire *et al*, 2004; Appendix Fig S4B and C) and blocker XE991 (Appendix Fig S4D and E) on PV's mIPSCs, we found that KCNQ

channels are indeed involved in the bidirectional regulation of PV's inhibition. Furthermore, co-application of XE991 with M1R antagonist Pir completely abolished the Pir-induced reduction in mIPSC frequency recorded at ZT0 (Appendix Fig S4F), indicating that KCNQ channels are critical downstream mediators of M1R activation in regulating PV's inhibition. In summary, we have found that ACh is involved in the daily regulation of PV's inhibitory synaptic transmission via targeting M1R, which then recruit KCNQ channels. This signaling pathway may serve as one important mechanism underlying the daily modulation of PV's neuronal function.

### Spontaneous activity of V1 L2/3 PV neurons oscillates naturally during the light/dark cycle in an experience-dependent manner

The balance between synaptic excitation (E) and inhibition (I) could dictate somatic firing (Liu, 2004; Gidon & Segev, 2012). The bidirectional oscillation in PV's E and I implies that PV neurons *in vivo* may have varied spontaneous activity at different times of the day. To test this hypothesis, we first performed *in vivo* two-photon calcium imaging to compare PV's spontaneous Ca<sup>2+</sup> activity at ZT0 and ZT12 (Fig 5A, Materials and Methods). The same group of L2/3 PV neurons in V1 was identified (Appendix Fig S5A) and we verified intermittent imaging would not disturb mice's regular activity cycle (Appendix Fig S5B). To avoid visual evoked response and eliminate the effect of arousal state on neural activity, imaging was conducted in dark with sufficient habituation while mice remained quietly awake and free-running in an air-suspended arena (Fig 5A<sub>3</sub>). We found that majority of PV neurons had higher spontaneous activity and more events at ZT12 compared to ZT0 (Fig 5B). The mean activity of all PV neurons (indicated by  $\text{sum}(\Delta F/F_0)$ , see Materials and Methods) was significantly larger with right-tilted cumulative distribution at ZT12 (Fig 5C). To further evaluate the detailed temporal profile of PV's spontaneous activity, we repetitively imaged mice four times in shuffled order at ZT0, 6, 12, and 18 with 36-h interval (Fig 5D). Consistent with the oscillatory patterns of sEPSCs and sIPSCs, most PV neurons had higher activity at ZT6 and/or 12 while reduced activity at ZT0 and/or 18 (Appendix Fig S5C), leading to an apparent oscillation of the mean activity across the 24-h day (Fig 5D). These distinct activity patterns are unlikely due to the relatively higher locomotor activity at ZT0 (Appendix Fig S6C) since no cross-correlation between neural activity and locomotion was found at either time point (Appendix Fig S6D). This is consistent with previous studies showing that the spontaneous activities of cortical PV neurons are either heterogeneously affected (Fu *et al*, 2014) or minimally affected especially for PV neurons localized in superficial cortical layers (Dipoppa *et al*, 2018) by locomotion. Hence, our *in vivo* findings support our hypothesis that the spontaneous activity of V1 PV neurons is naturally fluctuating during the day.

PV's synaptic excitation and inhibition are mainly regulated by experience and sleep, respectively, during the day. We next sought to investigate whether the daily oscillation of PV's spontaneous activity is influenced in similar ways (Fig 6A). 4 h of SD between ZT0 and ZT4 promoted activities of majority of the PV neurons (Fig 6B and C), which was largely prevented if sleep depriving in complete darkness (Fig 6D and E). These patterns resemble those of PV's sEPSCs (Fig 3H and Appendix Fig S2G), suggesting alike underlying mechanism. To summarize, experience plays a dominant role in modulating PV's excitatory input and spontaneous activity.

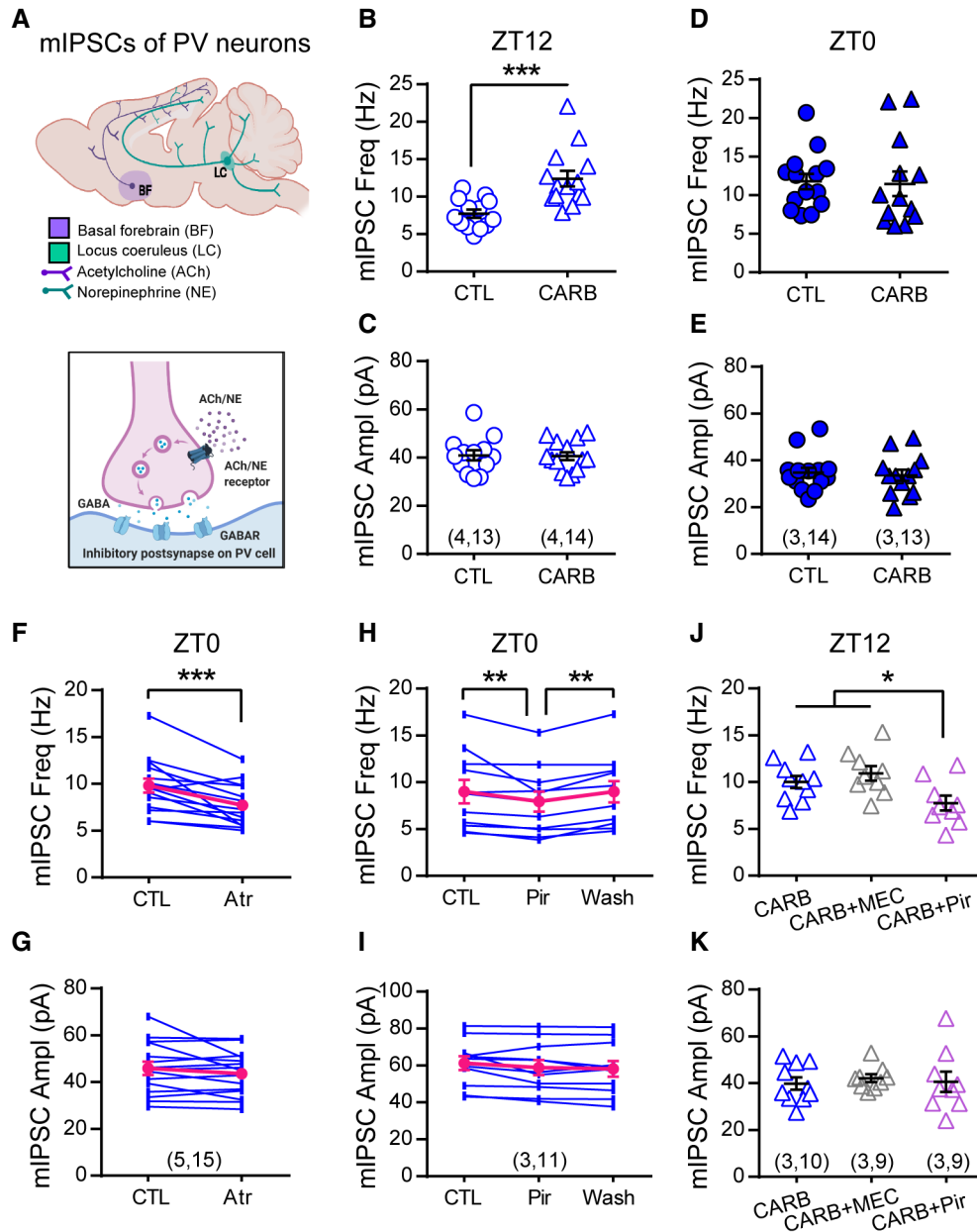


**Figure 4. Acetylcholine modulates inhibitory synaptic transmission of PV neurons via M1R during the day.**

**A** Diagram illustrating the potential neuromodulation of synaptic inhibition of PV neurons.

**B–E** Slices were obtained at ZT12 (**B–C**) or ZT0 (**D–E**) and pre-incubated with 50  $\mu$ M CARB for more than 1 h before recording mIPSCs in the presence of drug. Slices from the same animals were used as controls. CARB increased mIPSC frequency at ZT12 (CTL:  $7.74 \pm 0.55$  Hz; CARB:  $12.41 \pm 1.03$  Hz;  $P = 0.0001$ ; Mann–Whitney  $U$  test), but not ZT0 (CTL:  $11.79 \pm 1.00$  Hz; CARB:  $11.47 \pm 1.60$  Hz;  $P = 0.39$ ; Mann–Whitney  $U$  test). mIPSC amplitude was unchanged at either time (**C**, ZT12: CTL:  $40.94 \pm 2.08$  pA; CARB:  $40.64 \pm 1.66$  pA;  $P = 0.99$ ; **E**, ZT0: CTL:  $34.73 \pm 2.14$  pA; CARB:  $33.61 \pm 2.39$  pA;  $P = 0.85$ ; Mann–Whitney  $U$  test).

**F, G** mIPSC frequency (**F**, CTL:  $9.82 \pm 0.74$  Hz; Atr:  $7.70 \pm 0.57$  Hz;  $P = 0.0009$ ; Wilcoxon signed-rank test) and amplitude (**G**, CTL:  $45.88 \pm 2.87$  pA; Atr:  $43.64 \pm 2.40$  pA;  $P = 0.70$ ; Wilcoxon signed-rank test) recorded at ZT0 with acute atropine (Atr) wash on.

**H, I** Effect of acute wash-on and wash-off of pirenzepine (Pir) on mIPSC frequency (**H**, CTL:  $9.00 \pm 1.24$  Hz; Pir:  $7.94 \pm 1.07$  Hz; Washout:  $8.99 \pm 1.14$  Hz; One-way repeated measures ANOVA,  $F(2, 20) = 7.483$ ,  $P = 0.0037$ ; Holm–Sidak’s multiple comparison test) and amplitude (**I**, CTL:  $61.23 \pm 3.72$  pA; Pir:  $58.85 \pm 4.06$  pA; Washout:  $58.25 \pm 4.20$  pA; One-way repeated measures ANOVA,  $F(2, 20) = 3.197$ ,  $P = 0.0624$ ).

**J, K** Effect of pirenzepine or mecamylamine (MEC) on carbachol-induced elevation in mIPSC frequency at ZT12 (**J**, CARB:  $10.02 \pm 0.64$  Hz; CARB+MEC:  $10.95 \pm 0.78$  Hz; CARB+Pir:  $7.75 \pm 0.79$  Hz; One-way ANOVA,  $F(2, 25) = 4.848$ ,  $P = 0.0166$ ; Holm–Sidak’s multiple comparison test) and amplitude (**K**, CARB:  $39.85 \pm 2.60$  pA; CARB+MEC:  $42.17 \pm 1.65$  pA; CARB+Pir:  $40.67 \pm 4.34$  pA; One-way ANOVA,  $F(2, 25) = 0.1501$ ,  $P = 0.8614$ ).

Data information: Sample size is indicated as (mice, cells). Error bars in all figures indicate standard error of mean (s.e.m). The level of significance was set at  $P < 0.05$ .

\* $P < 0.05$ ; \*\* $P < 0.01$ ; \*\*\* $P < 0.001$ .

Source data are available online for this figure.

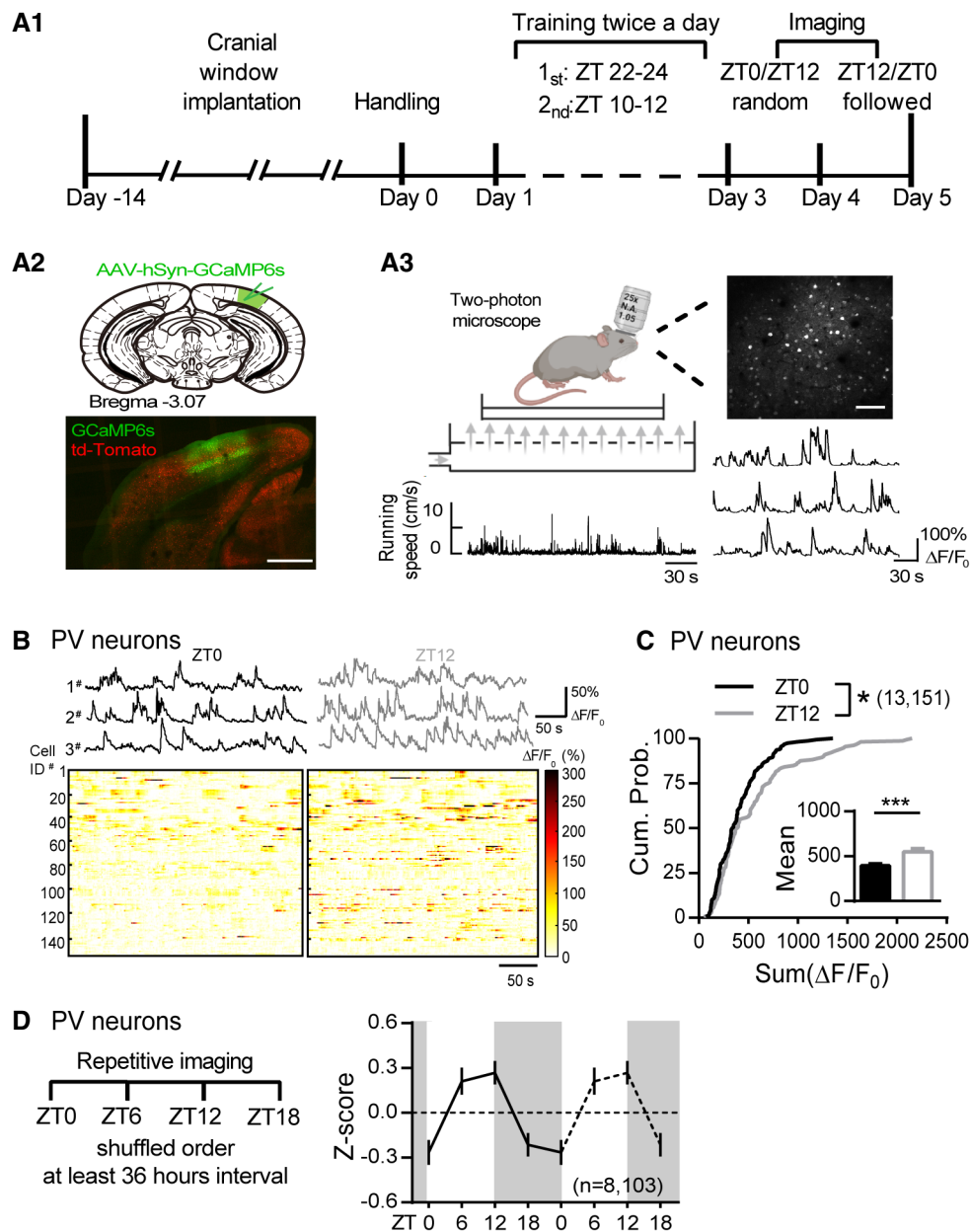


**Figure 5. Spontaneous activity of PV neurons oscillates naturally during the light/dark cycle.**

**A** A<sub>1</sub>. Diagram illustrating the *in vivo* two-photon imaging timeline. A<sub>2</sub>. GCaMP6s (green) was expressed in V1 of the PV: Ai9 mice (red: td-Tomato). Scale: 500  $\mu$ m. A<sub>3</sub>. Schematics of the calcium imaging showing a mouse that was head-fixed and free running on an air-suspended arena during the imaging section. Locomotor activity was simultaneously monitored (bottom left) along with Ca<sup>2+</sup> imaging (Top right. Scale: 100  $\mu$ m). Example spontaneous  $\Delta F/F_0$  traces (bottom right).

**B** Top panel, Example spontaneous  $\Delta F/F_0$  traces from three PV neurons repetitively imaged at ZT0 and ZT12. Bottom panels, Heatmaps showing the spontaneous  $\Delta F/F_0$  time-series traces of all PV neurons imaged at ZT0 and ZT12. The color code represents the magnitude of  $\Delta F/F_0$  (%).

**C** Cumulative probability distribution of the sum  $\Delta F/F_0$  of all PV neurons imaged at ZT0 and ZT12 (K-S test;  $P = 0.02$ ). Inset: the mean sum  $\Delta F/F_0$  (ZT0: 401.6 ± 19.55; ZT12: 559.1 ± 35.29;  $P = 0.0002$ ; Mann-Whitney U test). \*\*\* $P < 0.001$ .

**D** Left panel, diagram depicting repetitive imaging protocol. Right panel, mean activity of PV neurons indicated by Z score imaged at four timepoints.

Data information: Sample size is indicated as (mice, cells). Error bars in all figures indicate standard error of mean (s.e.m). The level of significance was set at  $P < 0.05$ . \* $P < 0.05$ ; \*\* $P < 0.01$ ; \*\*\* $P < 0.001$ .

Source data are available online for this figure.



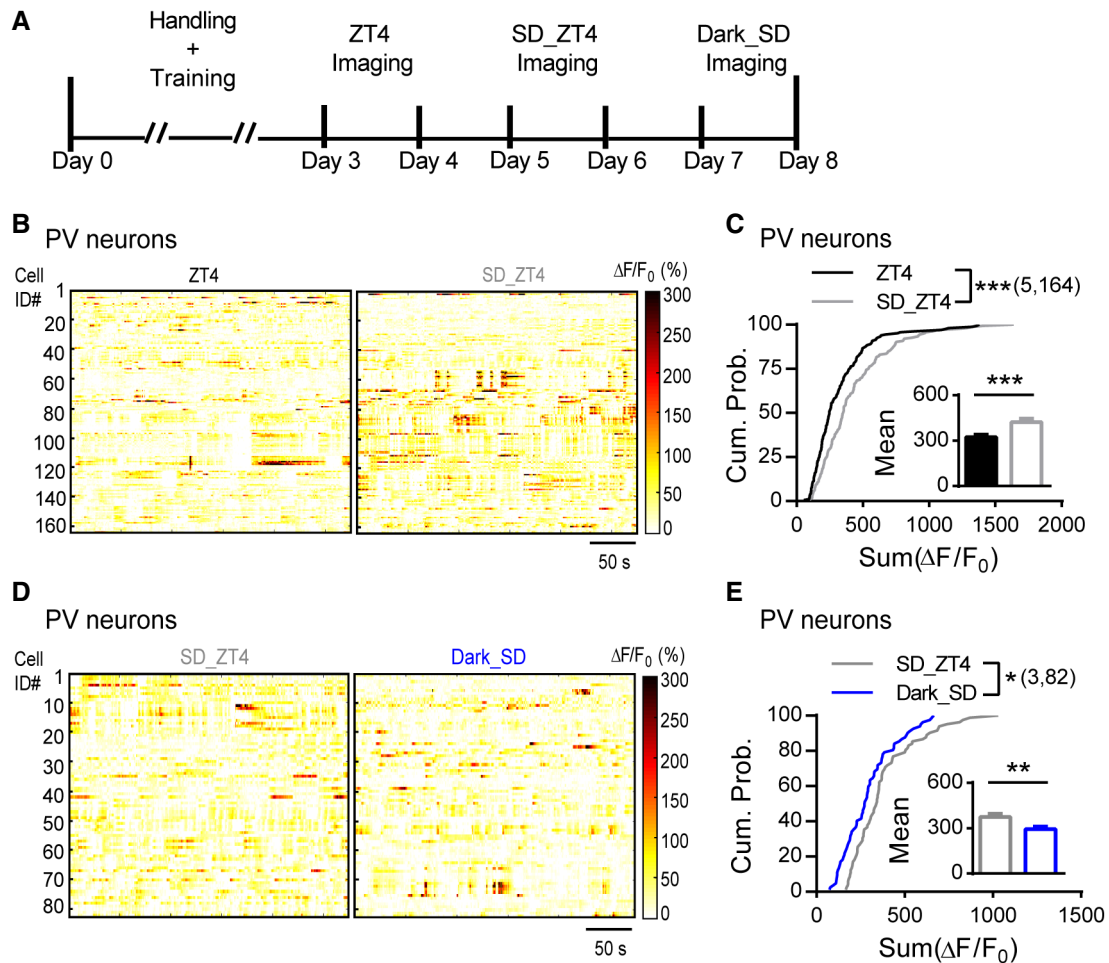


**Figure 6. PV neurons' daily activity rhythm relies on visual experience.**

A Diagram illustrating the timeline for repetitive imaging at ZT4, 4 h sleep deprivation (SD) from ZT0 to ZT4 (SD\_ZT4), and 4 h SD in darkness (Dark\_SD).  
 B Heatmaps showing the spontaneous  $\Delta F/F_0$  time-series traces of all PV neurons imaged at ZT4 and SD\_ZT4. The color code represents the magnitude of  $\Delta F/F_0$  (%).  
 C Cumulative probability distribution of the sum  $\Delta F/F_0$  of all PV neurons imaged at ZT4 and SD\_ZT4 (K-S test;  $P = 0.0001$ ). Inset: the mean sum  $\Delta F/F_0$  (ZT4:  $322.4 \pm 18.64$ ; SD\_ZT4:  $424.0 \pm 21.54$ ;  $P = 0.0004$ ; Mann-Whitney  $U$  test).  
 D Heatmaps showing the spontaneous  $\Delta F/F_0$  time-series traces of all PV neurons imaged at SD\_ZT4 and Dark\_SD. The color code represents the magnitude of  $\Delta F/F_0$  (%).  
 E Cumulative probability distribution of the sum  $\Delta F/F_0$  of all PV neurons imaged at SD\_ZT4 and Dark\_SD (K-S test;  $P = 0.015$ ). Inset: the mean sum  $\Delta F/F_0$  (SD\_ZT4:  $375.1 \pm 20.19$ ; Dark\_SD:  $293.8 \pm 16.55$ ;  $P = 0.0022$ ; Mann-Whitney  $U$  test).

Data information: Sample size is indicated as (mice, cells). Error bars in all figures indicate standard error of mean (s.e.m). The level of significance was set at  $P < 0.05$ .  $*P < 0.05$ ;  $**P < 0.01$ ;  $***P < 0.001$ .

Source data are available online for this figure.

### Daily modulation of PV neuronal function negatively correlates with activity cycle of pyramidal neurons and the altered dLGN-evoked responses in V1

In line with PV's higher activity (Fig 5) and greater inhibitory output (Fig 1) at ZT12 compared to ZT0, neighboring putative pyramidal neurons estimated by their  $Ca^{2+}$  response skewness (Dipoppa et al, 2018; Appendix Fig S6A) showed opposite change in activity as PV neurons (Fig 7A and B). Moreover, pyramidal cells displayed oscillatory activity during the 24-h day in the opposite direction as PV neurons (Fig 7C and Appendix Fig S6E), further supporting the physiological impact of PV's daily modulation.

PV neurons are key players regulating visual response gain. The high and low spontaneous activity of PV neurons that we observed during light and dark cycles, respectively, may be sufficient to alter the response gain. To test this possibility, we compared V1 responses evoked by stimulating dLGN at ZT0 and ZT12 from the same animals (Fig 7D<sub>1</sub>). We expressed Chr2-mCherry in dLGN neurons and GCaMP6s in V1 L2/3 neurons. An optic fiber was implanted laterally to deliver light stimulation over the dLGN neurons (Fig 7D<sub>2</sub>). 2–3 weeks after surgery, mice were habituated and repetitively imaged in complete darkness using two-photon microscopy under head-fixation at ZT0 and ZT12. We verified that our light stimulation could not induce visual-evoked responses

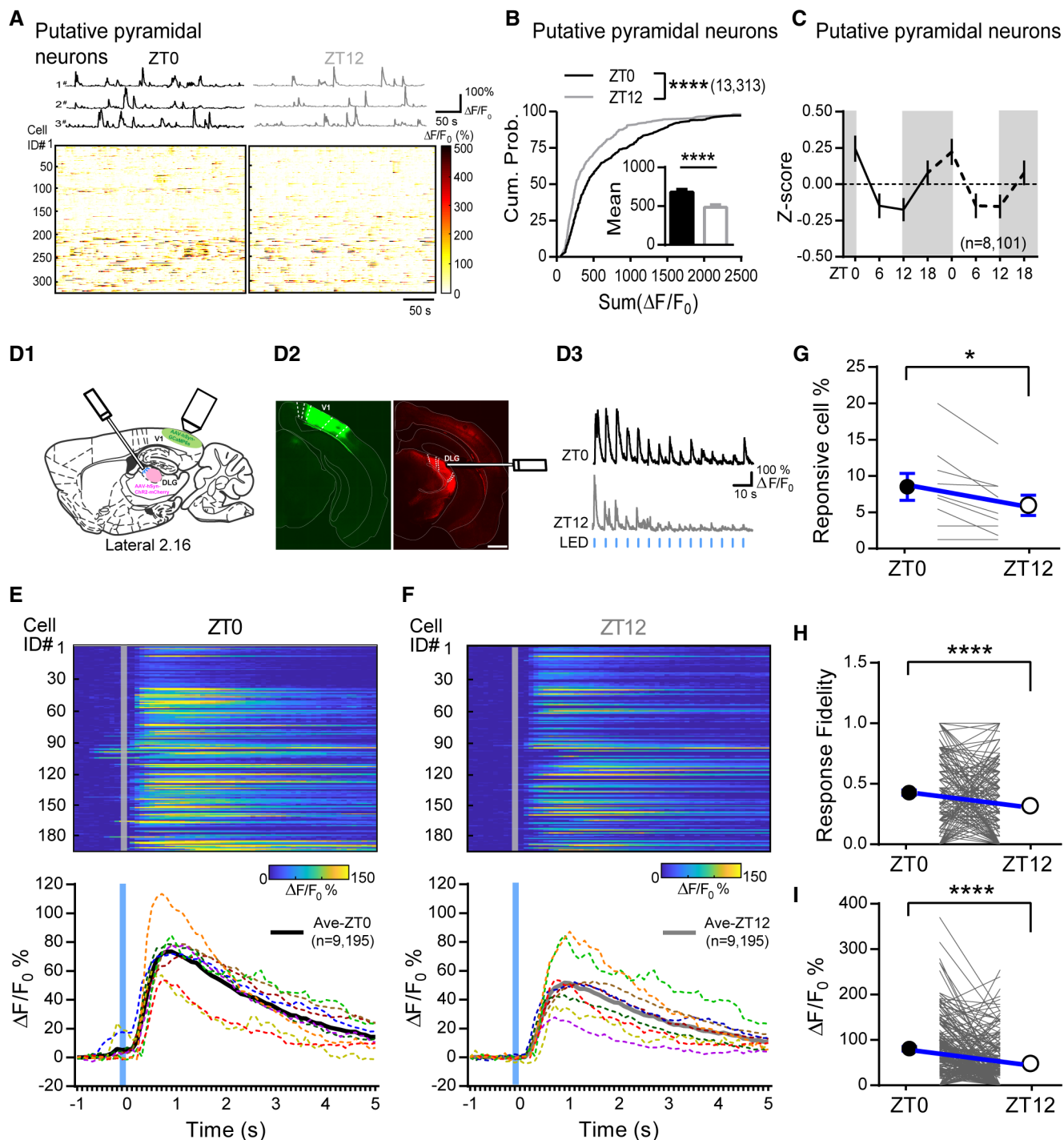


Figure 7.

(Appendix Fig S7A and B). Then we stimulated dLGN 15 times at 0.1 Hz and recorded evoked  $Ca^{2+}$  responses from the same population of neurons at both time points (Fig 7D<sub>3</sub>, see Materials and Methods). Not all neurons within the field of views (FOVs) had dLGN-evoked responses, but those showing responses at either or both time points were counted as the responsive cells and their percentages were calculated for each mouse. The dLGN-responsive cells are mostly putative pyramidal neurons. No PV neuron was

found to be responsive likely due to the small sample size or limited dLGN inputs were recruited. As expected, mice had a higher percentage of responsive cells when imaged at ZT0 compared to ZT12 (Fig 7G). The response fidelity of responsive cells, calculated as the proportion of evoked responses out of the 15 dLGN stimulations, was significantly higher at ZT0 than at ZT12 (Fig 7H). Finally, we compared the amplitude of the dLGN-evoked responses at both time points for each responsive cell and found larger responses at ZT0

**Figure 7. Pyramidal neurons have opposite daily oscillation and dLGN-evoked response is negatively correlated with PV's activity.**

- A Top panel, Example spontaneous  $\Delta F/F_0$  traces from three putative pyramidal neurons repetitively imaged at ZT0 and ZT12. Bottom panels, Heatmaps showing the spontaneous  $\Delta F/F_0$  time-series traces of all putative pyramidal neurons imaged at ZT0 and ZT12.
- B The cumulative distribution of the sum  $\Delta F/F_0$  of putative pyramidal neurons judged by skewness (K-S test;  $P < 0.0001$ ). Inset: the means of sum  $\Delta F/F_0$  (ZT0:  $679.5 \pm 38.22$ ; ZT12:  $485.8 \pm 32.22$ ;  $P < 0.0001$ ; Mann-Whitney  $U$  test).
- C Mean activity of putative pyramidal neurons indicated by Z score imaged at four timepoints.
- D D<sub>1</sub>, Schematic showing *in vivo* dLGN-evoked  $\text{Ca}^{2+}$  responses in V1. D<sub>2</sub>, Immunofluorescent staining showing the GCaMP6s (green) and ChR2-mCherry (red) expression in V1 and dLGN, respectively. The optical fiber track was also labeled. (Scale: 500  $\mu\text{m}$ ). D<sub>3</sub>, Response profile of an example neurons for dLGN stimulation during the light/dark cycle. Horizontal blue brief lines represent stimulus frequency.
- E–F Top: color-coded calcium signals of all responsive neurons (%  $\Delta F/F_0$ ). Bottom: The mean  $\text{Ca}^{2+}$  response waveform for individual mouse (dotted color lines) and all mice (thick black and gray lines). Trials were aligned to LED onset time (gray solid lines).
- G The fraction of neurons responsive to dLGN stimulus in ZT0 and ZT12. Each gray line represents one imaging mouse. Black and white circles and error bars represent the mean and SEM (ZT0:  $8.51 \pm 1.86$ ; ZT12:  $5.96 \pm 1.39$ ;  $P = 0.015$ ; Wilcoxon signed-rank test;  $n = 9$  mice).
- H The Response fidelity of each cell in ZT0 and ZT12. Black and white circles and error bars represent the mean and SEM (ZT0:  $0.42 \pm 0.022$ ; ZT12:  $0.31 \pm 0.023$ ;  $P < 0.0001$ ; Wilcoxon signed-rank test;  $n = 195$  cell).
- I Comparison of peak evoked response of each cell in ZT0 and ZT12. Black and white circles and error bars represent the mean and SEM (ZT0:  $81.01 \pm 4.79$ ; ZT12:  $48.42 \pm 3.82$ ;  $P < 0.0001$ ; Wilcoxon signed-rank test;  $n = 195$  cell).

Data information: Sample size is indicated as (mice, cells). Error bars in all figures indicate standard error of mean (s.e.m). The level of significance was set at  $P < 0.05$ .

\* $P < 0.05$ ; \*\* $P < 0.01$ ; \*\*\* $P < 0.001$ ; \*\*\*\* $P < 0.0001$ .

Source data are available online for this figure.

than at ZT12 (Fig 7E, F and I), which were inversely correlated with the spontaneous activity of local PV neurons (Appendix Fig S7C–F). Together, these results confirm that superficial neurons in V1 have greater dLGN-evoked responses at ZT0 than at ZT12, which is consistent with weaker PV activity during the dark and stronger activity during the light cycle. Thus, our data suggest that the daily modulation of PV neuronal function might be sufficient to impact the response gain in the visual cortex.

## Discussion

Proper function of PV neurons is critical for maintaining cognitive performance and highly relevant to a variety of brain disorders. Here we report that PV neurons in V1 are subjected to tight modulation during the natural light/dark cycle in a time- and sleep-dependent manners. ACh and its downstream M1R are critically involved in mediating this regulation. Changes in PV's activity *in vivo* negatively correlate with the activity pattern of surrounding pyramidal neurons and dLGN-evoked responses in V1, supporting the physiological significance of such daily modulation. Therefore, our study unveils a novel regulatory mechanism for PV neurons, provides implications on how daily rhythm, and sleep might modulate the brain function.

The inhibitory connections between PV and pyramidal neurons in cortices are known to be developmentally regulated in an experience-dependent manner (Jiang et al, 2005). However, in mature brain, inhibitory synapses become more stable and are resistant to experience deprivation (Gao et al, 2017). The lack of cortical iLTD in adult brain (Huang et al, 2010) suggests that these synapses are strongly anchored. Surprisingly, we found that the efficiency of the inhibitory connection between PV and pyramidal neurons dramatically differs between the light and dark cycle, consistent with our previous findings showing the upregulation and downregulation of mIPSC frequency of cortical pyramidal neurons (Bridi et al, 2020). These results imply that inhibitory synapses in adult brain are not as rigid as previously thought, but instead are flexibly modulated during the 24-h day. The exact mechanism underlying

this daily modulation remains to be examined. One possibility is that the lower inhibition at ZT12 might enhance PV's output by reducing the activation threshold of PV neurons.

The bidirectional changes in PV's excitatory and inhibitory synaptic transmission show strong time dependency. Both of them rapidly transit from high to low or vice versa after entering the next cycle, and then they remain relatively stable throughout the rest of the cycle regardless of similar sleep/wake activity (Fig 3B and C), suggesting a time-dependent regulation. Circadian rhythm has long been proposed to regulate synaptic efficacy, especially the excitatory synapses of excitatory neurons (Frank & Cantera, 2014). We previously found that the inhibitory synaptic strength of cortical pyramidal neurons also shows rhythmicity (Bridi et al, 2020). Hence, inhibitory synaptic efficacy of both excitatory and inhibitory neurons is likely under circadian modulation as excitatory synapses. In addition to circadian rhythm, much evidence supports the role of sleep in regulating excitatory synaptic plasticity (Tononi & Cirelli, 2020). Indeed, we found that sleep directly regulates the transition of PV's inhibitory synaptic transmission during the early light cycle. Interestingly, the gradually decreased sIPSCs during the light cycle temporally coincides with the reduction in slow wave activity (SWA; Appendix Fig S2H and I), which is widely used to measure the sleep pressure (Huber et al, 2000), further implying a connection between sleep and PV's synaptic modulation. Therefore, the daily modulation of PV's synaptic transmission is dependent on both time and sleep. We further identified that ACh via M1R activation is critical signal mediating the bidirectional modulation of PV's inhibitory synaptic efficacy. Interestingly, the working dynamic of the same cholinergic signaling seems to be different for upregulation and downregulation of PV's mIPSCs. High mIPSCs at ZT0 can be rapidly reduced by blocking the ACh-M1R signal (Fig 4F and H), while low mIPSCs at ZT12 requires prolonged activation of this pathway (Fig 4B and Appendix Fig S3D). This distinction suggests that chronic high level of cortical ACh is critical for maintaining the inhibitory synaptic efficacy onto PV neurons during the dark cycle. However, when cholinergic tone is low during the late light cycle, these inhibitory synapses are more resistant to abrupt increases in ACh induced by interspersed wake and rapid eye movement (REM)

sleep episodes (Marrosu *et al*, 1995; Ma *et al*, 2020). Neuromodulators are candidates mediating both the sleep- and time-dependent synaptic regulation (Frank & Cantera, 2014; TONONI & Cirelli, 2014). The circadian rhythm of cortical ACh level (Kametani & Kawamura, 1991; Jiménez-Capdeville & Dykes, 1993) well correlates with the daily modulation of PV's inhibitory synapses, which can account for both its sleep and time dependency. Thus, our results provide evidence supporting the active role of ACh in the daily regulation of the inhibitory synapses specifically onto PV neurons.

It is surprising to find that the ACh-dependent regulation of mIPSCs is unique for PV but not pyramidal neurons in V1 L2/3 (Appendix Fig S3H) even though they receive inhibition from overlapping resources (Harris & Mrsic-Flogel, 2013). This might be due to the unique enrichment of M1Rs at presynaptic terminals targeting PV neurons. The diversity of subtypes and subcellular distribution of neuromodulator receptors have long been known (Dembrow & Johnston, 2014; Palomero-Gallagher & Zilles, 2019). For example, it has been shown that nAChR activation selectively potentiates the thalamocortical but not the intracortical synapses of L3 pyramidal neurons in the primary somatosensory cortex (Gil *et al*, 1997). A recent study reported that the neuron-derived neurotrophic factor (NDNF)-expressing interneurons in V1 L1 specifically target supragranular PV neurons (Cohen-Kashi Malina *et al*, 2021), which could be another explanation for the selectivity of ACh. On the other hand, we have not examined other neuromodulators such as serotonin and histamine, both of which have dense innervation in the visual cortex and also show rhythmic brain levels (Kosofsky *et al*, 1984; Manning *et al*, 1996). Their potential contribution cannot be excluded, although our results do suggest manipulating cholinergic signaling alone is sufficient to bidirectionally alter PV's mIPSCs.

In V1, PV's opposite oscillations in E and I temporally coincide with their spontaneous activity *in vivo*, which is congruent with the role of E/I ratio in controlling somatic firing (Gidon & Segev, 2012). Indeed, PV's activity was greatly modified by SD via directly altering visual experience similar as their excitatory inputs. Therefore, PV's spontaneous activity likely shares similar time- and sleep-dependent regulation during the day and the circadian rhythm of the cholinergic signaling may also be involved. Although this hypothesis remains to be tested, it provides one explanation to reconcile the discrepancy regarding the role of acute sleep stages and/or sleep history in modulating neuronal firing (Vyazovskiy *et al*, 2009; Grosmark *et al*, 2012; Hengen *et al*, 2013; Mizuseki & Buzsaki, 2013; Miyawaki & Diba, 2016; Niethard *et al*, 2016; Watson *et al*, 2016). When studies are conducted during the early light cycle, sleep and sleep history indeed alter neuronal firing (Vyazovskiy *et al*, 2009; Grosmark *et al*, 2012; Miyawaki & Diba, 2016; Niethard *et al*, 2016; Watson *et al*, 2016), probably due the sleep-dependent changes in cortical levels of ACh as well as other neuromodulators (Hasselmo, 1999; Nadim & Bucher, 2014; Bridi *et al*, 2020), and neuronal properties such as synaptic efficacy have not yet reached steady state. For others examining neuronal firing during the late light cycle when the tone of most neuromodulators remains low and the neuronal properties are already stable, switching between sleep stages or even sleep history may not be sufficient to cause changes (Hengen *et al*, 2013; Mizuseki & Buzsaki, 2013). All these studies suggest that sleep and time may interact dynamically, resulting in complex regulation of neural activity that will demand more in-depth investigation to disentangle the underlying mechanisms.

Our results suggest different mean activity between the light and dark cycle for PV and putative pyramidal neurons, which seems to be contradictory to previous findings showing similar mean firing rate of regular spiking neurons between the cycles (Hengen *et al*, 2016). This might be due to sampling bias. While we only studied neurons in supragranular layers at static timepoints, their multiunit recording usually targeted neurons in deeper cortical layers over long period of time. It is necessary to point out that the mean activity of non-PV non-putative pyramidal neurons are not different between ZT0 and ZT12 (Appendix Fig S6F and G), further suggesting cell type-specific dynamic of neural activity. In addition, we have only shown time-dependent changes in neural activity when mice were quietly awake, which may partially reflect the effect of sleep history but not acute sleep stages. PV neurons in somatosensory cortex are found to fire at higher rate at wake and REM sleep compared to NREM sleep during the early light cycle (Niethard *et al*, 2016). Opposite findings are recently reported (Brecier *et al*, 2022). How PV neurons in V1 are modulated by acute sleep stages and how PV neurons in other cortical regions are modulated daily remains to be examined.

PV neurons play a critical role in gain control. Their daily oscillation in neural activity may cause the neural network where they reside in to respond differentially to their inputs (Ferguson & Cardin, 2020), which may underlie the daily fluctuation in cognitive performance (Muto *et al*, 2016). Studies in the visual cortex have provided solid evidence to show that PV's activity determines the gain of visual response (Wilson *et al*, 2012; Zhu *et al*, 2015). Although the magnitude of PV oscillation is not as great as the optogenetic manipulation used previously (Atallah Bassam *et al*, 2012), they may be sufficient to alter the response gain in V1. Indeed, the dLGN-evoked responses in V1 are significantly different between ZT0 and ZT12 following the gain rule of PV neurons, strongly suggesting that the daily modulation of PV neuronal function is physiologically important. It is worthy of notice that PV's impact on both spontaneous and evoked activity in V1 seems to be restricted to the normal physiological conditions. Both activity of pyramidal neurons and dLGN-evoked responses were elevated after 4 h of SD (Appendix Fig S8) when PV's activity was also increased (Fig 6B and C). These results suggest that under disturbed conditions such as SD, modulation of neural activity as well as dLGN-V1 connection may utilize complex mechanisms in addition to PV's inhibition. For example, SD may directly facilitate dLGN-V1 synapses by recruiting neuromodulatory signal (Kuo & Dringenberg, 2008) such as histamine (Soya *et al*, 2008).

In the visual circuit, light sensitivity of retina has long been known to show circadian rhythm (Bassi & Powers, 1986) and arousal state influences the retina output (Schroder *et al*, 2020). Here we directly activated dLGN neurons to mimic visual input; therefore, we could exclude the potential contribution of retina to the alternating V1 responses. Recently, dLGN neural activity is found to be rhythmically regulated (Chrobok *et al*, 2021). It remains to be evaluated whether the rhythmic change in dLGN activity may also affect V1 responses at different times of the day. Other consequences of PV's daily modulation remain to be investigated. Some recent studies reported that both layer 5 cortical pyramidal neurons (Krone *et al*, 2021) and somatostatin neurons in prefrontal cortex (preprint: Tossell *et al*, 2020) are directly involved in sleep regulation. It will be interesting to



examine whether PV's daily changes may also have regulatory role for sleep via unknown circuitries.

Additionally, our findings also provide some mechanistic implications for neuronal dysfunction in brain diseases such as AD. Impaired PV neuronal function is considered a key abnormality in AD brains (Verret et al, 2012; Cattaud et al, 2018), which is linked to reduced gamma oscillation and impaired cognitive performance (Verret et al, 2012; Palop & Mucke, 2016). Meanwhile, disturbed sleep and circadian rhythm and impaired cholinergic function are commonly observed in AD patients, which could be initiated decades before the diagnosis and are recognized as risk factors for AD (Falgas et al, 2021). Here by showing how synaptic and neuronal properties of PV neurons are diurnally regulated, we provide new direction to investigate how AD-associated PV's dysregulation might be triggered.

## Materials and Methods

### Animals

All experimental procedures were approved by the Institutional Animal Care and Use Committees at the Interdisciplinary Research Center on Biology and Chemistry, Chinese Academy of Science. Homozygous PV-ires-cre mice (B6;129P2-Pvalb<sup>tm1(cre)Arbr</sup>/J, PV:cre, Jax Laboratory) were used in this study. They were either crossed with Ai9 mice (B6.Cg-Gt(ROSA)26Sor<sup>tm9(CAG-tdTomato)Hze</sup>/J, Jax Laboratory) to genetically label PV neurons with tdTomato (PV: Ai9), or with Ai32 mice (B6;129S-Gt(ROSA)26Sor<sup>tm32(CAG-COP4\*H134R/EYFP)Hze</sup>/J, Jax Laboratory) to express channelrhodopsin-2 (ChR2) and EYFP specifically in PV neurons (PV: Ai32). 5- to 10-week-old male mice were used only. All mice were housed with a 12 h:12 h light/dark cycle with *ad libitum* access to food and water. Mice with shifted light/dark cycle were entrained in customized entrainment chamber for at least 2 weeks before experiments. The light-on time (ZT0) was adjusted according to the experiment.

### Acute brain slices preparation

300  $\mu$ m thickness acute coronal brain slices containing the primary visual cortex or motor cortex were prepared as described previously. Briefly, mice were anesthetized with isoflurane vapor and rapidly sacrificed within 2 h before the light on (ZT0) or light off (ZT12). Slices were cut in ice-cold dissection buffer containing the following: 212.7 mM sucrose, 5 mM KCl, 1.25 mM NaH<sub>2</sub>PO<sub>4</sub>, 10 mM MgCl<sub>2</sub>, 0.5 mM CaCl<sub>2</sub>, 26 mM NaHCO<sub>3</sub>, and 10 mM dextrose, bubbled with 95% O<sub>2</sub>/5% CO<sub>2</sub>. Slices were transferred and incubated at 30°C for 30 min with artificial cerebrospinal fluid (ACSF) containing 119 mM NaCl, 5 mM KCl, 1.25 mM NaH<sub>2</sub>PO<sub>4</sub>, 1 mM MgCl<sub>2</sub>, 2 mM CaCl<sub>2</sub>, 26 mM NaHCO<sub>3</sub>, and 10 mM dextrose, saturated with 95% O<sub>2</sub> and 5% CO<sub>2</sub>. After that, slices were maintained at room temperature (RT) for at least 30 min before recording.

### Whole-cell recording

Whole-cell recordings were made from the tdTomato-expressed PV neurons in layer 2/3 of V1 or M1. Slices were submerged in the

recording chamber perfused with 30  $\pm$  0.5°C perfusion buffer at 2 ml/min. Cells were visualized by an upright fluorescence microscope (Olympus XT640-W). Borosilicate glass pipette recording electrodes with 3–5 M $\Omega$  resistance were filled with different internal solutions according to the experiment, all of which were adjusted to pH 7.3–7.4, 285–300 mOsm. Data were filtered at 2 kHz and digitized at 10 kHz using Digidata 1550A (Molecular Devices, CA, USA). Only cells with input resistant Ri  $\geq$  100 M $\Omega$  and access resistance Ra  $\leq$  25 M $\Omega$  were used for analysis. In addition, cells were discarded if Ri and Ra changed more than 25% during the recording.

### Miniature postsynaptic current recordings

For mEPSC recordings, 1  $\mu$ M TTX, 100  $\mu$ M DL-APV and 20  $\mu$ M gabazine were added to the ACSF to isolate AMPAR-mediated mEPSCs. The internal solution contained 8 mM KCl, 125 mM cesium gluconate, 10 mM HEPES, 1 mM EGTA, 4 mM MgATP, 0.5 mM NaGTP, 10 mM Na-phosphocreatine, and 5 mM QX-314. Cells were held at –80 mV.

For mIPSC recordings, 1  $\mu$ M TTX, 100  $\mu$ M DL-APV, and 20  $\mu$ M CNQX were added into the bath. The internal solution contained 8 mM NaCl, 120 mM cesium chloride, 10 mM HEPES, 2 mM EGTA, 4 mM MgATP, 0.5 mM NaGTP, and 10 mM QX-314. Cells were held at –80 mV for experiments in Fig 2 and –60 mV for those in Fig 4 and Appendix Figs S3 and S4.

### Spontaneous postsynaptic current recordings

Spontaneous EPSCs were recorded in regular ACSF without any blocker. Cells were held at –55 mV, the measured reversal potential of the inhibitory current (Appendix Fig S2A). To record spontaneous IPSCs, ACSF containing 100  $\mu$ M DL-APV and 20  $\mu$ M CNQX was used and cells were held at –60 mV during the recording. Internal solution for sEPSC and sIPSC was similar to those used for mEPSC and mIPSC except no QX-314 was added.

### ChR2-assisted mapping of the connectivity between PV and pyramidal neurons

Acute brain slices containing V1 from PV: Ai32 mice were prepared. L2/3 pyramidal neurons were identified by their morphologies and voltage clamped at –50 mV with the same internal solution and perfusion buffer as mIPSC recording. A 0.45 mm<sup>2</sup> square region surrounding the recorded neuron was divided into 15 by 15 grids. Brief blue light pulses (10 ms at 100% intensity with 1 s inter-stimulus interval) were controlled by Polygon400 (Mightex, USA) and delivered via a water immersion objective (10 $\times$ , 0.30 NA, Olympus) to each grid in a fixed pseudo-random order and repeated three times. Light-evoked inhibitory postsynaptic currents (<sub>LE</sub>IPSC) were recorded.

### Whole-cell current clamp recording of light-evoked action potential

Acute brain slices containing V1 from 5- to 8-week-old male PV: Ai32 mice were prepared as described above. PV neurons were identified by the EYFP and current clamped with glass pipette filled with internal solution containing 130 mM K-gluconate, 10 mM KCl, 10 mM HEPES, 0.2 mM EGTA, 0.5 mM NaGTP, 4 mM MgATP, 10 mM Na-phosphocreatine. Action potential was evoked by trains of 5 ms 470 nm blue light pulses (Lumen Dynamics) at varied frequency for 1 s.



### Sleep deprivation

Mice were kept awake by gentle handling, during which EEG/EMG signals were acquired simultaneously.

### Polysomnography recording and analysis

Five- to six-week-old PV: Ai9 mice were anesthetized by 1–2% isoflurane vapor and head-fixed. The skull was exposed. Two epidural screws were implanted (B: –1 to 2 mm, L: 2 to 3 mm) as EEG electrodes. Two resin-insulated stainless-steel wires bared at the tip region were implanted into the dorsal neck muscles and sutured in place to record the EMG. All electrodes were connected to a 4-pin socket connector that was glued to the skull by dental cement. After surgery, the wound was treated with triple antibiotic ointment and mice were allowed to recover in their home cage for at least 7 days before the experiment. Mice were transferred to the customized chamber at least 48 h before the recording for habituation.

During recording, EEG and EMG signals were sampled at 1,024 Hz with 1,000 times preamplifier gain and bandpass filtered at EEG: 0.3–1,000 Hz, EMG: 1–5,000 Hz. All signals were acquired by Spike Hound.

States of wakefulness, NREM, and REM sleep were first automatically analyzed in 10-s epoch by Neuro Score (Data Sciences International) using the preconfigured protocol. EMG was used to discriminate between wake and sleep. EMG threshold was manually defined for each mouse. Epochs with more than 20% of the absolute EMG samples above the threshold were classified as wakefulness. In addition, slow wave ratio ( $\delta$  power/total power) was used to discriminate between NREM sleep (with ratio  $\geq 0.4$ ) and wake/REM sleep (with ratio  $< 0.4$ ). Theta ratio ( $\theta$  power/total power) was used to discriminate REM sleep (with ratio  $\geq 3$ ) from other sleep stages (with ratio  $< 3$ ). All automatic analyses were visually confirmed. Amount of time spent in each of three arousal states (NREM, REM, and wakefulness) was quantified. NREM and REM sleep amount were added up as total sleep time. Time spent in wake and sleep were then compared between groups.

### Corticosterone measurement

Blood was collected during acute brain slice dissection for both *ad libitum* sleep and SD mice. Blood was then incubated at RT for 2 h and centrifuged at 2,000 g for 20 min at 4°C to isolate serum. The corticosterone levels were measured by corticosterone ELISA kit.

### Visual deprivation

PV: Ai9 mice entrained to the regular light/dark cycle were allowed to habituate to the customized light-proof, well-ventilated entrainment chambers in their homecages at least 2 days before the experiment. Visual deprivation was achieved by keeping one group of mice in the dark during the last light cycle before they were sacrificed for experiment.

### Immunohistochemistry

Mice were perfused with ice-cold 1× PBS and 4% paraformaldehyde (PFA) and fixed overnight in 4% PFA. 50  $\mu$ m coronal slices were

cut with a vibratome (Lecia, VT1000s) and preserved in cryoprotectant solution (30% sucrose, 20% ethylene glycol and 50% 1× PBS) at –20°C before used. Before staining, slices were washed with 1× PBS followed by 2 h incubation with blocking solution containing 5% normal goat serum (Sigma, USA) and 0.1% Triton X-100 in 1× PBS at RT. After that, slices were incubated with primary antibody diluted with blocking solution overnight at 4°C. Slices were then washed with 1× PBS with 0.1% Tween 20, 15 min/time for three times and once more with 1× PBS. Slices were incubated with secondary antibody diluted with blocking solution for 2 h at RT. The washing steps were repeated again and slices were mounted on glass slide and air-dried overnight. At last, mounting medium (Prolong gold antifade reagent, Invitrogen) was added on slices to preserve fluorescence signal before confocal imaging. Antibodies used include: GFP polyclonal chicken antibody (1:1,000, Abcam, ab13970); GAD 65 monoclonal mouse antibody (1:1,000, Abcam, ab26113); Goat anti-chicken Alexa Fluor 488 (1:1,000, Thermo Fisher, A-11039); and Goat anti-mouse Alexa Fluor 488 (1:1,000, Abcam, ab150113). Images were acquired by a spinning disk microscope (Andor) with 20× air objective.

### Virus injection and cranial window preparation

Six- to eight-week-old PV: Ai9 mice were maintained anesthetized by 1–2% isoflurane vapor and head-fixed in a stereotaxic frame. Ophthalmic ointment (Cisen, China) was applied to the eyes and mice were kept on a heating pad where the temperature was maintained at around 37°C. Skin was sterilized by iodine and a craniotomy was made above the right visual cortex. A 3 × 3 mm circular piece of skull was removed (3.0 mm post the bregma suture, 2.0 mm from the mild line suture) and the dura was kept intact and moist with sterile saline. 50–100 nl AAV2-hSyn-GCaMP6s ( $1 \times 10^{12}$  genome copies per ml, Taitool, China) was delivered using a beveled glass pipette by a microsyringe pump (Stoelting, USA) at 30 nl/min. Total 4–5 injections were made at a depth of ~250  $\mu$ m in the primary visual cortex. After the virus injection, a cover glass was glued to the skull over the circular opening by using polyacrylic glue (Elmer's, USA). A customized headplate was then cemented to the skull around the center of the cranial window. Skin was sutured back around the headplate and lidocaine (Sigma, USA) and triple antibiotic ointment (DearGo, China) were applied around the wound. Mice were transferred back to their homecages after fully recovered from anesthesia and were closely monitored during the following week. Virus was allowed to expressed for at least 14 days before the experiment.

### *In vivo* two-photon calcium imaging

The whole procedure was illustrated in Fig 5A. Specifically, all mice were gently handled 5–10 min for 2–3 times between ZT0–4 on day 0. From days 1 to 3, mice were allowed to habituate to the head fixation and free running in the mobile homecage (Neurotar, Finland) under the two-photon microscopy twice a day, 1 h each between ZT10–12 and ZT22–24. All mice were imaged at least twice (ZT0 and ZT12) post-training. Some mice were repeatedly imaged four times at ZT0, ZT6, ZT12, and ZT18 with shuffled order. All imaging sections were spaced out with at least 36 h interval, during which mice were housed in their homecages with activity monitored by video.

For each imaging section, mice were head-fixed under the microscopy at least 10 min before the imaging started. Imaging was performed using a two-photon laser-scanning microscope (FVMPE-RS, OLYMPUS) coupled with a Mai Tai Insight DS Dual-OL laser (Spectra Physics). The tunable laser was set to 920 nm (~30–70 mW average power on the sample) for GCaMP6s and the 1,040 nm laser was used for exciting the tdTomato. The emission filter set consisted of a 570 nm dichroic mirror and a 540/50 nm band-pass filter. Fluorescence was detected using GaAsP photomultiplier tubes. Images of  $512 \times 512$  pixels (x/y resolution: 0.663  $\mu\text{m}/\text{pixel}$ ) were scanned in a line mode repeated three times by a resonant galvanometer and 3,000–6,000 frames were acquired at 10 Hz for each field of view (FOV). The locomotor activity of all mice during all imaging section was monitored with Motion Tracker (Neurotar, Finland) and/or camera.

To image the same population of neurons across sections, the same FOV was tracked by vascular features, cortical depth, and spatial location of landmarks (bright and stable structures of somas). Only neurons showing clear and similar cell morphology were included for analysis.

### Estimation of locomotor activity

For locomotion monitored with Motion tracker (Neurotar, Finland), the locomotion was measured by travel speed in cm/s and travel distance (cm). For mice monitored by camera, the locomotor activity was analyzed post-hoc by EthoVision XT (Noldus 11.5).

### dLGN optogenetic manipulations

500 nl AAV2-hSyn-hChr2(H134R)-mCherry virus or AAV2-hSyn-mCherry-WPRE (Taitool) was injected into the right dLGN with stereotaxic atlas (AP -2.3; ML 2.15; DV 2.5;  $\angle 90^\circ$ ) at a rate of 50 nl/min. A 200  $\mu\text{m}$  OD optical fiber (NA = 0.37, Inper) was implanted lateral over dLGN with the same coordination. Cranial window over the right primary visual cortex was prepared and AAV virus expressing GCaMP6s was injected into the superficial layer of V1 as describe above. The recovery and habituation were similar as the regular two-photon imaging. Optogenetic stimulation of dLGN was achieved using a 470 nm Fiber-Coupled LED (Thorlabs, M470F3) controlled by a LED Driver (Thorlabs, DC2200). Black ceramic sleeve was used to prevent the light from leaking. Light intensity at the fiber tip was set at 75–80 mW/mm<sup>2</sup> and 10 ms light pulses were delivered at 0.1 Hz for 15 trials. The GCaMP6s signal was acquired in the same way as described in the above section. At the end of experiment, animals were sacrificed and 50  $\mu\text{m}$  coronal brain slices were sectioned with a vibratome to confirm the position of optic fiber an Chr2 expression (Fig 7D<sub>2</sub>).

### Quantification and statistical analysis

#### Whole-cell recordings

##### Miniature postsynaptic currents

mEPSCs and mIPSCs were analyzed using the MiniAnalysis program (Synaptosoft, Decatur, GA) as described previously (Bridi et al, 2020). Event detection threshold was set at three times over the RMS noise. At least 300 events with rise time  $\leq 3$  ms for mEPSCs and  $\leq 5$  ms for mIPSCs were selected for each cell to

calculate frequency and amplitude. And non-overlapping events were used to construct the average trace and estimate the decay time.

##### Spontaneous postsynaptic currents

Spontaneous EPSCs and IPSCs were analyzed by calculating the unit charge (nA/s) with customized code (MATLAB, MathWorks) as described previously (Bridi et al, 2020). Briefly, the root mean square (RMS) noise of each 500 msec segment was calculated and subtracted. Charge was calculated as the integral of the post-subtracted signal of total 3–4 min of recording.

##### Chr2-assisted mapping of the connectivity between PV and pyramidal neurons

The max amplitude of the response evoked within 30 msec time window post-light stimulation was measured. Only reliably evoked responses (2 out of 3 repeats) larger than 60 pA were considered as <sub>LE</sub>IPSCs and the mean was used as the measurement of the connection strength. A heatmap showing the connection strength for each recorded neuron was generated. Maps from each group were either aligned by the patched cell soma (soma-align) or slice pia (pia-align). For soma alignment, maps from the same group were simply averaged since the relative soma position of the recorded neuron was the same across maps. For pia alignment, the 369  $\times$  680 pixels DIC image showing the shape of the cortical slice, the 15 by 15 grids, and the position of the recording electrode using the 10 $\times$  objective was taken at the end of each recording. The variation in cortical thickness was first corrected by scaling individual DIC image to match that in the reference image (ref, Fig 1A<sub>3</sub> top right). The amplitude of the <sub>LE</sub>IPSCs was used to define the pixel values for the corresponding grid in the scaled image. Then the pia in the ref was aligned with that of the scaled DIC image and the pixel value was projected onto the ref. After projecting <sub>LE</sub>IPSCs from all neurons, the average was calculated for each pixel in the reference image and the pia-aligned map was generated and compared between ZT0 and ZT12. All analyses were done by Clampfit (Molecular Devices, CA, USA) and customized matlab programs.

##### Calcium image analysis

Images were analyzed *post-hoc* using customized matlab programs modified based on the original open-source package available online (<https://github.com/flatironinstitute/CalmAn-MATLAB>). Briefly, stacked time-series images were registered by aligning to a target image using a cross-correlation-based registration algorithm (discrete Fourier transformation, DFT, algorithm) to correct brain motion (Xin et al, 2019). The target image was obtained by mean projection of visually identified frames ( $\geq 200$  frames) with few motion artifacts. Regions of interest (ROIs) were drawn for individual neuron manually based on neuronal shape using a customized GUI and the raw fluorescence signal ( $F$ ) for all ROIs from all frames was extracted. To calculate  $\Delta F/F_0$ , the initial 200 frames for each cell were excluded to avoid imaging artifact.

$$\Delta F/F_0 = (F - F_0)/F_0$$

Baseline fluorescence ( $F_0$ ) was computed via a sliding-window (400 frames for PV neurons and 550 frames for non-PV neurons) using a 30% quantile cutoff. The correlation coefficient ( $R^2$ )

between the converted  $\Delta F/F_0$  waveform and the raw  $F$  waveform was calculated and only cells with  $R^2$  larger than 0.70 were included for final analysis.

To estimate neural activity from the calcium signals, the sum of  $\Delta F/F_0$  (sum( $\Delta F/F_0$ )) was calculated after subtracting the three times of the minimal RMS noise of each cell.

### Light-evoked $Ca^{2+}$ signal analysis

The dLGN-evoked  $Ca^{2+}$  responses in the superficial layer of V1 was calculated as  $(F-F_0)/F_0 \times 100\%$ . The average of the 10 frames (1 s) before the onset of light stimulation was used as  $F_0$ . The peak  $Ca^{2+}$  intensity within the 1 s time window following stimulus onset was measured as the  $F$ . Only responses larger than 15% were included for final analysis. To analyze the fraction of responsive neurons, neurons showing at least one effective response at either ZT0 or 12 were counted and divided to the total neurons that had detectable spontaneous activity within the FOV. Response fidelity for each responsive neuron was calculated as the proportion of evoked responses out of the 15 stimuli.

### Statistics

For all figures, the sample size is indicated as (mice, cells) or otherwise specified. Statistical analysis was performed by Prism V6.0 software (GraphPad Software, Inc.). Wilcoxon signed-rank test was used for two paired groups analysis. Mann–Whitney  $U$  test was used for two unpaired groups analysis. For more than three unpaired groups analysis, one-way ANOVA followed by Holm–Sidak’s multiple comparison test was used. For acute drug wash-on and off recordings from the same neuron, one-way repeated measures ANOVA followed by Holm–Sidak’s multiple comparison test was used. Cumulative distributions were compared with the Kolmogorov–Smirnov (K-S) test. Error bars in all figures indicate standard error of mean (s.e.m). Only significant comparisons were labeled in the figures. The level of significance was set at  $P < 0.05$ .  $*P < 0.05$ ;  $**P < 0.01$ ;  $***P < 0.001$ ;  $****P < 0.0001$ .

## Data availability

The customized MATLAB codes are available on Github [<https://github.com/KaiWen-Helab/Matlab-code/tree/master>].

**Expanded View** for this article is available [online](#).

### Acknowledgments

We thank Dr. Junying Yuan, Dr. Alfredo Kirkwood, Dr. Aaron Gitler for insightful discussion. This work is supported by NSFC (Grant No. 32070963, 31700917), Shanghai Science and Technology Development Foundation (Grant No. 22ZR1475100), and Shanghai Municipal Science and Technology Major Project (Grant No. 2019SHZDX02) to K-WH.

### Author contributions

**Fang-jiao Zong:** Data curation; formal analysis; investigation; methodology; writing – original draft. **Xia Min:** Investigation; methodology.

**Yan Zhang:** Software; formal analysis. **Xue-Ting Zhang:** Investigation.

**Yang Liu:** Validation; investigation. **Yu-Ke Li:** Validation; investigation.

**Kai-Wen He:** Conceptualization; resources; supervision; funding acquisition;

investigation; visualization; methodology; writing – original draft; project administration; writing – review and editing.

### Disclosure and competing interests statement

The authors declare that they have no conflict of interest.

## References

- Atallah Bassam V, Bruns W, Carandini M, Scanziani M (2012) Parvalbumin-expressing interneurons linearly transform cortical responses to visual stimuli. *Neuron* 73: 159–170
- Bassi CJ, Powers MK (1986) Daily fluctuations in the detectability of dim lights by humans. *Physiol Behav* 38: 871–877
- Brecier A, Borel M, Urbain N, Gentet LJ (2022) Vigilance and behavioral state-dependent modulation of cortical neuronal activity throughout the sleep/wake cycle. *J Neurosci* 42: 4852–4866
- Bridi MCD, Zong FJ, Min X, Luo N, Tran T, Qiu J, Severin D, Zhang XT, Wang G, Zhu ZJ et al (2020) Daily oscillation of the excitation-inhibition balance in visual cortical circuits. *Neuron* 105: e4
- Cattaud V, Bezzina C, Rey CC, Lejards C, Dahan L, Verret L (2018) Early disruption of parvalbumin expression and perineuronal nets in the hippocampus of the Tg2576 mouse model of Alzheimer’s disease can be rescued by enriched environment. *Neurobiol Aging* 72: 147–158
- Choy JMC, Agahari FA, Li L, Stricker C (2018) Noradrenaline increases mEPSC frequency in pyramidal cells in layer II of rat barrel cortex via calcium release from presynaptic stores. *Front Cell Neurosci* 12: 213
- Chrobok L, Jeczmiern-Lazur JS, Pradel K, Klich JD, Bubka M, Wojcik M, Kepczynski M, Lewandowski MH (2021) Circadian actions of orexins on the retinorecipient lateral geniculate complex in rat. *J Physiol* 599: 231–252
- Cohen-Kashi Malina K, Tsivourakis E, Kushinsky D, Apelblat D, Shtiglitz S, Zohar E, Sokoletsky M, Tasaka GI, Mizrahi A, Lampl I et al (2021) NDNF interneurons in layer 1 gain-modulate whole cortical columns according to an animal’s behavioral state. *Neuron* 109: 2150–2164
- Dembrow N, Johnston D (2014) Subcircuit-specific neuromodulation in the prefrontal cortex. *Front Neural Circuits* 8: 54
- Dipoppa M, Ranson A, Krumin M, Pachitariu M, Carandini M, Harris KD (2018) Vision and locomotion shape the interactions between neuron types in mouse visual cortex. *Neuron* 98: 602–615
- Falgas N, Walsh CM, Neylan TC, Grinberg LT (2021) Deepen into sleep and wake patterns across Alzheimer’s disease phenotypes. *Alzheimers Dement* 17: 1403–1406
- Faradji-Prevautel H, Cespuglio R, Jouvett M (1990) Circadian rest-activity rhythms in the anophthalmic, monocular and binocular ZRDC/an mice. Retinal and serotonergic (raphe) influences. *Brain Res* 526: 207–216
- Ferguson KA, Cardin JA (2020) Mechanisms underlying gain modulation in the cortex. *Nat Rev Neurosci* 21: 80–92
- Frank MG, Cantera R (2014) Sleep, clocks, and synaptic plasticity. *Trends Neurosci* 37: 491–501
- Fu Y, Tucciarone JM, Espinosa JS, Sheng N, Darcy DP, Nicoll RA, Huang ZJ, Stryker MP (2014) A cortical circuit for gain control by behavioral state. *Cell* 156: 1139–1152
- Gao M, Whitt JL, Huang S, Lee A, Mihalas S, Kirkwood A, Lee HK (2017) Experience-dependent homeostasis of ‘noise’ at inhibitory synapses preserves information coding in adult visual cortex. *Philos Trans R Soc Lond B Biol Sci* 372: 20160156

- Gidon A, Segev I (2012) Principles governing the operation of synaptic inhibition in dendrites. *Neuron* 75: 330–341
- Gil Z, Connors BW, Amitai Y (1997) Differential regulation of neocortical synapses by neuromodulators and activity. *Neuron* 19: 679–686
- Grosmark AD, Mizuseki K, Pastalkova E, Diba K, Buzsaki G (2012) REM sleep reorganizes hippocampal excitability. *Neuron* 75: 1001–1007
- Han EB, Stevens CF (2009) Development regulates a switch between post- and presynaptic strengthening in response to activity deprivation. *Proc Natl Acad Sci U S A* 106: 10817–10822
- Harris KD, Mrsic-Flogel TD (2013) Cortical connectivity and sensory coding. *Nature* 503: 51–58
- Hasselmo ME (1999) Neuromodulation: acetylcholine and memory consolidation. *Trends Cogn Sci* 3: 351–359
- Hengen KB, Lambo ME, Van Hooser SD, Katz DB, Turrigiano GG (2013) Firing rate homeostasis in visual cortex of freely behaving rodents. *Neuron* 80: 335–342
- Hengen KB, Torrado Pacheco A, McGregor JN, Van Hooser SD, Turrigiano GG (2016) Neuronal firing rate homeostasis is inhibited by sleep and promoted by wake. *Cell* 165: 180–191
- Hijazi S, Heistek TS, Scheltens P, Neumann U, Shimshek DR, Mansvelter HD, Smit AB, van Kesteren RE (2019) Early restoration of parvalbumin interneuron activity prevents memory loss and network hyperexcitability in a mouse model of Alzheimer's disease. *Mol Psychiatry* 25: 3380–3398
- Hu H, Gan J, Jonas P (2014) Interneurons. Fast-spiking, parvalbumin(+) GABAergic interneurons: From cellular design to microcircuit function. *Science* 345: 1255263
- Hu JS, Vogt D, Sandberg M, Rubenstein JL (2017) Cortical interneuron development: a tale of time and space. *Development* 144: 3867–3878
- Huang S, Gu Y, Quinlan EM, Kirkwood A (2010) A refractory period for rejuvenating GABAergic synaptic transmission and ocular dominance plasticity with dark exposure. *J Neurosci* 30: 16636–16642
- Huber R, Deboer T, Tobler I (2000) Effects of sleep deprivation on sleep and sleep EEG in three mouse strains: empirical data and simulations. *Brain Res* 857: 8–19
- Jelitai M, Puggioni P, Ishikawa T, Rinaldi A, Duguid I (2016) Dendritic excitation-inhibition balance shapes cerebellar output during motor behaviour. *Nat Commun* 7: 13722
- Jiang B, Huang ZJ, Morales B, Kirkwood A (2005) Maturation of GABAergic transmission and the timing of plasticity in visual cortex. *Brain Res Brain Res Rev* 50: 126–133
- Jiménez-Capdeville ME, Dykes RW (1993) Daily changes in the release of acetylcholine from rat primary somatosensory cortex. *Brain Res* 625: 152–158
- Jones CE, Opel RA, Kaiser ME, Chau AQ, Quintana JR, Nipper MA, Finn DA, Hammock EAD, Lim MM (2019) Early-life sleep disruption increases parvalbumin in primary somatosensory cortex and impairs social bonding in prairie voles. *Sci Adv* 5: eaav5188
- Jurgensen S, Castillo PE (2015) Selective dysregulation of hippocampal inhibition in the mouse lacking autism candidate gene CNTNAP2. *J Neurosci* 35: 14681–14687
- Kametani H, Kawamura H (1991) Circadian rhythm of cortical acetylcholine release as measured by *in vivo* microdialysis in freely moving rats. *Neurosci Lett* 132: 263–266
- Kerlin AM, Andermann ML, Berezovskii VK, Reid RC (2010) Broadly tuned response properties of diverse inhibitory neuron subtypes in mouse visual cortex. *Neuron* 67: 858–871
- Kosofsky BE, Molliver ME, Morrison JH, Foote SL (1984) The serotonin and norepinephrine innervation of primary visual cortex in the cynomolgus monkey (*Macaca fascicularis*). *J Comp Neurol* 230: 168–178
- Krone LB, Yamagata T, Blanco-Duque C, Guillaumin MCC, Kahn MC, van der Vinne V, McKillop LE, Tam SKE, Peirson SN, Akerman CJ et al (2021) A role for the cortex in sleep-wake regulation. *Nat Neurosci* 24: 1210–1215
- Kruglikov I, Rudy B (2008) Perisomatic GABA release and thalamocortical integration onto neocortical excitatory cells are regulated by neuromodulators. *Neuron* 58: 911–924
- Kuo MC, Dringenberg HC (2008) Histamine facilitates *in vivo* thalamocortical long-term potentiation in the mature visual cortex of anesthetized rats. *Eur J Neurosci* 27: 1731–1738
- Liu G (2004) Local structural balance and functional interaction of excitatory and inhibitory synapses in hippocampal dendrites. *Nat Neurosci* 7: 373–379
- Liu BH, Li P, Li YT, Sun YJ, Yanagawa Y, Obata K, Zhang LI, Tao HW (2009) Visual receptive field structure of cortical inhibitory neurons revealed by two-photon imaging guided recording. *J Neurosci* 29: 10520–10532
- Liu ZW, Faraguna U, Cirelli C, Tononi G, Gao XB (2010) Direct evidence for wake-related increases and sleep-related decreases in synaptic strength in rodent cortex. *J Neurosci* 30: 8671–8675
- Ma X, Zhang Y, Wang L, Li N, Barkai E, Zhang X, Lin L, Xu J (2020) The firing of theta state-related septal cholinergic neurons disrupt hippocampal ripple oscillations via muscarinic receptors. *J Neurosci* 40: 3591–3603
- Manning KA, Wilson JR, Uhrlich DJ (1996) Histamine-immunoreactive neurons and their innervation of visual regions in the cortex, tectum, and thalamus in the primate *Macaca mulatta*. *J Comp Neurol* 373: 271–282
- Marin O (2012) Interneuron dysfunction in psychiatric disorders. *Nat Rev Neurosci* 13: 107–120
- Marrosu F, Portas C, Mascia MS, Casu MA, Fà M, Giagheddu M, Imperato A, Gessa GL (1995) Microdialysis measurement of cortical and hippocampal acetylcholine release during sleep-wake cycle in freely moving cats. *Brain Res* 671: 329–332
- Martire M, Castaldo P, D'Amico M, Preziosi P, Annunziato L, Tagliatela M (2004) M channels containing KCNQ2 subunits modulate norepinephrine, aspartate, and GABA release from hippocampal nerve terminals. *J Neurosci* 24: 592–597
- Miyawaki H, Diba K (2016) Regulation of hippocampal firing by network oscillations during sleep. *Curr Biol* 26: 893–902
- Mizuseki K, Buzsaki G (2013) Preconfigured, skewed distribution of firing rates in the hippocampus and entorhinal cortex. *Cell Rep* 4: 1010–1021
- Murthy VN, Schikorski T, Stevens CF, Zhu Y (2001) Inactivity produces increases in neurotransmitter release and synapse size. *Neuron* 32: 673–682
- Muto V, Jaspas M, Meyer C, Kusse C, Chellappa SL, Degueldre C, Baiteau E, Shaffii-Le Bourdieu A, Luxen A, Middleton B et al (2016) Local modulation of human brain responses by circadian rhythmicity and sleep debt. *Science* 353: 687–690
- Nadim F, Bucher D (2014) Neuromodulation of neurons and synapses. *Curr Opin Neurobiol* 29: 48–56
- Niethard N, Hasegawa M, Itokazu T, Oyanedel CN, Born J, Sato TR (2016) Sleep-stage-specific regulation of cortical excitation and inhibition. *Curr Biol* 26: 2739–2749
- Palomero-Gallagher N, Zilles K (2019) Cortical layers: Cyto-, myelo-, receptor- and synaptic architecture in human cortical areas. *Neuroimage* 197: 716–741
- Palop JJ, Mucke L (2016) Network abnormalities and interneuron dysfunction in Alzheimer disease. *Nat Rev Neurosci* 17: 777–792
- Rudy B, Fishell G, Lee S, Hjerling-Leffler J (2011) Three groups of interneurons account for nearly 100% of neocortical GABAergic neurons. *Dev Neurobiol* 71: 45–61

- Sadeh S, Clopath C (2021) Inhibitory stabilization and cortical computation. *Nat Rev Neurosci* 22: 21–37
- Schroder S, Steinmetz NA, Krumin M, Pachitariu M, Rizzi M, Lagnado L, Harris KD, Carandini M (2020) Arousal modulates retinal output. *Neuron* 107: e9
- Soya A, Song YH, Kodama T, Honda Y, Fujiki N, Nishino S (2008) CSF histamine levels in rats reflect the central histamine neurotransmission. *Neurosci Lett* 430: 224–229
- Steullet P, Cabungcal JH, Coyle J, Didriksen M, Gill K, Grace AA, Hensch TK, LaMantia AS, Lindemann L, Maynard TM et al (2017) Oxidative stress-driven parvalbumin interneuron impairment as a common mechanism in models of schizophrenia. *Mol Psychiatry* 22: 936–943
- Sur M, Nagakura I, Chen N, Sugihara H (2013) Mechanisms of plasticity in the developing and adult visual cortex. *Prog Brain Res* 207: 243–254
- Tononi G, Cirelli C (2014) Sleep and the price of plasticity: from synaptic and cellular homeostasis to memory consolidation and integration. *Neuron* 81: 12–34
- Tononi G, Cirelli C (2020) Sleep and synaptic down-selection. *Eur J Neurosci* 51: 413–421
- Tossell K, Yu X, Soto BA, Vicente M, Miracca G, Giannos P, Miao A, Hsieh B, Ma Y, Yustos R, Vyssotski AL, Constandinou T, Franks NP, Wisden W (2020) Sleep deprivation triggers somatostatin neurons in prefrontal cortex to initiate nesting and sleep via the preoptic and lateral hypothalamus. *bioRxiv* <https://doi.org/10.1101/2020.07.01.179671> [PREPRINT]
- Verret L, Mann EO, Hang GB, Barth AM, Cobos I, Ho K, Devidze N, Masliah E, Kreitzer AC, Mody I et al (2012) Inhibitory interneuron deficit links altered network activity and cognitive dysfunction in Alzheimer model. *Cell* 149: 708–721
- van Versendaal D, Levelt CN (2016) Inhibitory interneurons in visual cortical plasticity. *Cell Mol Life Sci* 73: 3677–3691
- Vogt D, Cho KKA, Shelton SM, Paul A, Huang ZJ, Sohal VS, Rubenstein JLR (2018) Mouse Cntnap2 and human CNTNAP2 ASD alleles cell autonomously regulate PV<sup>+</sup> cortical interneurons. *Cereb Cortex* 28: 3868–3879
- Vyazovskiy VV, Olcese U, Lazimy YM, Faraguna U, Esser SK, Williams JC, Cirelli C, Tononi G (2009) Cortical firing and sleep homeostasis. *Neuron* 63: 865–878
- Wang JJ, Li Y (2016) KCNQ potassium channels in sensory system and neural circuits. *Acta Pharmacol Sin* 37: 25–33
- Wang Y, Xu C, Xu Z, Ji C, Liang J, Wang Y, Chen B, Wu X, Gao F, Wang S et al (2017) Depolarized GABAergic signaling in Subicular microcircuits mediates generalized seizure in temporal lobe epilepsy. *Neuron* 95: e5
- Watson BO, Levenstein D, Greene JP, Gelinis JN, Buzsaki G (2016) Network homeostasis and state dynamics of neocortical sleep. *Neuron* 90: 839–852
- Wilson NR, Runyan CA, Wang FL, Sur M (2012) Division and subtraction by distinct cortical inhibitory networks *in vivo*. *Nature* 488: 343–348
- Xin Y, Zhong L, Zhang Y, Zhou T, Pan J, Xu NL (2019) Sensory-to-category transformation via dynamic reorganization of ensemble structures in mouse auditory cortex. *Neuron* 103: e6
- Zhu Y, Qiao W, Liu K, Zhong H, Yao H (2015) Control of response reliability by parvalbumin-expressing interneurons in visual cortex. *Nat Commun* 6: 6802